

AARTFAAC Flux Density Calibration and Northern Hemisphere Catalogue at 60 MHz

Mark Kuiack,^{1*} Folkert Huizinga,¹ Gijs Molenaar,³ Peeyush Prasad,¹
 Antonia Rowlinson,^{1,2} Ralph A.M.J. Wijers¹

¹ Anton Pannekoek Institute, University of Amsterdam, Science Park 904, 1098 XH Amsterdam, The Netherlands

³ Department of Physics and Electronics, Rhodes University, PO Box 94, Grahamstown, 6140, South Africa

² ASTRON, The Netherlands Institute for Radio Astronomy, Postbus 2, 7990 AA, Dwingeloo, The Netherlands

Accepted XXX. Received YYY; in original form ZZZ

ABSTRACT

We present a method for calibrating the flux density scale for images generated by the Amsterdam ASTRON Radio Transient Facility And Analysis Centre (AARTFAAC). AARTFAAC produces a stream of all-sky images at a rate of one second in order to survey the Northern Hemisphere for short duration, low frequency transients, such as the prompt EM counterpart to gravitational wave events, magnetar flares, blazars, and other as of yet unobserved phenomena. Therefore, an independent flux density scaling solution per image is calculated via bootstrapping, comparing the measured apparent brightness of sources in the field to a reference catalogue. However, the lack of accurate flux density measurements of bright sources below 74 MHz necessitated the creation of the AARTFAAC source catalogue, at 60 MHz, which contains 167 sources across the Northern Hemisphere. Using this as a reference results in a sufficiently high number of detected sources in each image to calculate a stable and accurate flux scale per one second snapshot, in real-time.

Key words: Surveys – Catalogues – Radio Continuum: Transients – Radio Continuum: General – Methods: Data Analysis

1 INTRODUCTION

The Amsterdam ASTRON Radio Transient Facility And Analysis Center (AARTFAAC) is an all-sky radio monitor, built as a parallel computational back-end to LOFAR (the Low-Frequency Array; van Haarlem et al. 2013). It operates primarily in LOFAR’s low band (10 – 90 MHz) with an all-sky field of view, but can also operate in the high band (110 – 240 MHz) albeit only with an HBA tile field of view (30° FWHM at 150 MHz). It can be used to monitor the radio sky on time scales upwards of one second, as often as is practicable within LOFAR observing constraints and data storage limitations. Its core science goal is to search for rare, bright transients at the lowest radio frequencies, which have proved to be quite elusive (see, e.g., Bell et al. 2014; Obenberger et al. 2015; Rowlinson et al. 2016; Carbone et al. 2016), but a few have been found in the otherwise poorly explored regime accessible to AARTFAAC (Hyman et al. 2005; Stewart et al. 2016; Murphy et al. 2017): time scales of sec-

onds to hours, and fluxes above several jansky in the LOFAR low band (10 – 90 MHz). In this regime, coherently emitting objects will dominate, and thus any sources found will represent fairly extreme or exotic physics; (see, e.g., Pietka et al. 2015).

However, many other applications are possible, such as detecting very high-redshift EoR signals (Patil et al. 2017), monitoring the state of the ionosphere and phenomena in it (Loi et al. 2015a,c), and monitoring meteor showers (e.g., Obenberger et al. 2014). And of course, many terrestrial phenomena such as RFI, air planes, and satellites are detected that need to be distinguished from more distant astrophysical signals and imaging artifacts before science analysis can start.

At the moment, AARTFAAC all-sky monitoring is limited to times when LOFAR is in LBA mode¹, but more importantly, due to the fact that the search for interesting objects has not yet been automated, and storage and offline

* E-mail: m.j.kuiack@uva.nl

¹ An upgrade is planned and funded that will allow simultaneous LBA and HBA observations

search of the very large volumes of raw data it generates is not practical. In this paper, we describe the next step in achieving the goal of continuous all-sky monitoring with AARTFAAC. Previously, we described the basic properties of the AARTFAAC system and its real-time calibration and technical commissioning (Prasad et al. 2014), as well as the system design and correlator (Prasad et al. 2016), and TraP, the transients detection pipeline also used for LOFAR transient searches (Swinbank et al. 2015). In this paper, we describe the results of the first practical commissioning runs. The basic goal of these runs was to collect enough data to cover the full range of local sidereal times over a significant period of time (so as to cover a range of ionospheric and RFI conditions) to investigate practical strategies of bad data rejection, source extraction, and flux calibration to enable future real-time operation. We collected over 30 hours of data, which we will show is a good compromise between getting a manageable dataset to experiment with extensively and sampling a sufficient range of conditions. In future work, we will first develop strategies for separating events of interest in large datasets from artifacts and known variability, before implementing the full intended data analysis (data taking, correlation, calibration, imaging, flux extraction, feature recognition, and alert generation) into a streaming pipeline that can function in real-time.

To increase the sensitivity to fainter objects, the brightest sources in the sky: Cygnus A, Cassiopeia A, Taurus A, Virgo A, The Sun, hereafter referred to as the “A-team”, and most of the diffuse Galactic plane emission, is removed during AARTFAAC calibration and imaging. The images have, thus far, not yet been properly flux calibrated (Prasad et al. 2014). Instead the pixel values in the resulting images are relative, with a scaling related to a normalization of the total power received before “A-team” subtraction. An accurate characterization of transient phenomena however, requires reference to a common physical scale. While studies of variability also require that each extracted source measurement is made within a comparable reference frame. This is only possible once each image has been corrected such that the pixel values refer to the physical units of flux density, janskys.

Radio flux density calibration is done by reference to catalogues of stable, well studied calibrator sources. For example, a typical radio observation includes observing a calibrator source before and after observing the target. So the scaling of the calibrator data, the gain solution, is applied to the target data. In that case the gain solution is assumed not to have changed substantially on the timescale of the observation.

Unfortunately for AARTFAAC, the only large surveys below 100 MHz are The Very Large Array Low-frequency Sky Survey Redux (VLSSr; Lane et al. 2014) at 74 MHz and The Eighth Cambridge (8C) Survey (Rees 1990) at 38 MHz. There is therefore a gap across nearly the entire frequency range of AARTFAAC. This clearly represents an opportunity for AARTFAAC to make an important contribution, with unique flux density measurements of the brightest sources in the 38 – 74 MHz range.

We therefore report on the method used to flux density calibrate AARTFAAC images in real-time, for our future transient search campaigns, and the resulting catalogue of bright sources.

Firstly, in Section 2 particular technical details of AARTFAAC and the calibration observations are given. Secondly, in Section 3 we describe the catalogue bootstrapping method used to accurately flux density calibrate the images in real-time. Then, we report on the performance and stability of the method in section 4, and analyses of the typical systematic uncertainties. Next in Section 5 the characteristics of the first AARTFAAC catalogue of persistent sources at 60 MHz are discussed. And lastly conclusions are given in section 6.

2 DATA DESCRIPTION

By creating an all-sky image every second, AARTFAAC has the capability of generating a large amount of data. Therefore, the intended operational mode is to perform a transient search on the stream of images, saving only those data where an interesting event has been detected. However, in order to test the calibration method and fully characterize the data quality a set of observations was recorded and stored for analysis offline.

Additionally, full LST coverage was required to generate the catalogue of calibrator sources across the Northern Hemisphere. Therefore, nearly 33 hours of observations were recorded to test the flux density calibration method and generate the AARTFAAC catalogue. This allowed the analysis of sources for many hours, across separate observations, while maintaining a manageable data volume. These observations were recorded between August and December of 2016, as outlined in Table 1. During this period of time the final stages of commissioning with the real-time imaging pipeline were completed, leaving only the image calibration.

In its present form the AARTFAAC system shares the 6 core stations, known as the “Superterp,” with LOFAR, which is located near the village of Exloo in the Netherlands. It was designed to operate in parallel with regular LOFAR observations by splitting the antenna signals from the stations and rerouting them to the AARTFAAC correlators and imaging servers.

Each core LOFAR station consists of two sub arrays: the High Band Array (HBA), which has a bandpass from 120-240 MHz, and the Low Band Array (LBA), with a bandpass from 10-90 MHz. AARTFAAC currently only uses the LBA.

These LBA stations are made of 96 pairs of orthogonal droop dipoles distributed with a roughly Gaussian density distribution. Their simple antenna design, two wires attached at 45 degrees to a central post over a metal mesh ground plane, offer a full sky field of view. Unfortunately, due to current computational constraints only data from 48 of the 96 antennas are processed. This subset of antennas may be distributed in one of 4 operating modes:

- INNER: Antennas within 30 meters of the station centre.
- OUTER: Antennas 30 to 87 meters.
- 2 SPARSE modes: Either odd or even numbered antennas distributed throughout the station.

LOFAR LBA observes predominately in the OUTER configuration due to the larger number of longer baselines providing better UV filling of the superterp. In comparison using the INNER configuration results in dipoles which

Start Date	Start - End [UTC]	Start - End [LST]	Good Images #	Un-flagged data %
2016 Aug 31	15:10 - 17:43	14h18m - 16h52m	8839	96.3
2016 Sep 05	16:47 - 19:45	16h15m - 19h14m	10358	97.0
2016 Sep 07	03:40 - 09:38	03h14m - 09h14m	21291	99.1
2016 Sep 30	09:31 - 11:23	10h36m - 12h29m	2703	40.2
2016 Nov 12	06:32 - 19:53	10h26m - 23h50m	40145	83.5
2016 Nov 13	20:00 - 22:57	00h01m - 02h58m	5031	47.4
2016 Nov 14	08:27 - 15:33	09h03m - 16h56m	23084	90.3
2016 Dec 10	22:55 - 02:49	04h43m - 08h37m	9794	70.0
Total	32:56:46		121245	

Table 1. The set of observations used to test the flux density calibration method and generate the first AARTFAAC catalogue at 60 MHz. The start and end of each observation are given as the UTC of the first and last image, as well as the LST centre of the image, both to the nearest minute. During an observation data blocks may be flagged and removed either by the correlator, visibility calibration, or imaging pipeline. Then, the images were filtered based on the average image pixel RMS. Outliers are clearly the result of improper calibration, poor A-team subtraction, or bright RFI.

are more tightly clumped in the centre of the station, leaving more space between the stations. The OUTER configuration utilizes the outer ring of station dipoles which maximizes point source sensitivity and reduces diffuse background emission. Additionally, regular LOFAR LBA observations will sum the antenna signals with a phase delay applied for the target pointing. However, because these phase delays are not applied at the stations during LBA observations, AARTFAAC has access to the raw signal from all 48 dipoles in operation, and is sensitive to the entire visible sky during all LBA observations.

The physical specifications of AARTFAAC are summarized in Table 2. Currently, in the standard operating mode of AARTFAAC a one second integrated Stokes I (1024x1024 resolution, 4.1 MB) fits image is created every second by integrating all 16 available subbands. This is a reduction from the initial total raw visibility rate 660 MB/s, including all subbands, which is reduced to 10 MB/s after calibration by averaging the 63 frequency channels which comprise each LOFAR subband. These calibrated visibilities are stored in the AARTFAAC archive for offline processing, and the upcoming transient survey. However, in the future only those data which are found to contain an interesting transient event will be stored.

In order to maximize sensitivity while reducing RFI, the subbands are configured in two continuous sets of eight subbands, 57.52 - 59.08 MHz and 61.04 - 62.6 MHz. This is near enough the peak sensitivity around 57 MHz (van Haarlem et al. 2013), while avoiding frequencies which have been observed to have a higher RFI occupancy percentage, (see Fig. 6, Offringa et al. 2013). With this configuration a pixel RMS < 10 Jy is achieved over 40% of the Northern Hemisphere, while 90% achieves RMS < 21 Jy.

3 IMAGE CALIBRATION

The AARTFAAC real-time calibration and imaging pipelines, as they are currently implemented, output all sky snapshot images at a rate, and integration time, of one second (Prasad et al. 2014). Yet, before the images can be used for transient detection or variability analysis, two corrections

must be made: First, a direction dependent rescaling, which corrects the images based on the antenna response pattern, also known as the primary beam. Then, a direction independent rescaling, which transforms the pixel values from arbitrary units to a flux density in janskys.

Both of these corrections are important before the image stream can be analyzed for transient or variable sources. Clearly, without accounting for any variation in the antenna response across the sky, where sensitivity peaks at zenith, the brightness of all sources would appear variable as they track across the field of view.

Similarly, applying a reliable flux density scaling to each image is vital for measuring variability. Given that the pixel values in raw images are arbitrary, with an unknown influence from the subtraction of the A-team sources, it would be difficult to determine whether any variation is intrinsic or an artifact of the calibration and imaging. Furthermore, searching for a transient source in an image with arbitrary scaling would make it impossible to determine the shape of the light curve, spectral index, or whether a candidate is indeed astrophysical at all.

These characteristics are also critical when devising further observations as they dictate what sensitivity and spectral coverage are necessary to maximize the likelihood of a follow-up detection. Additionally, in the cases where detections are made but follow-up observations yield no result, the shape and flux density distributions of transient light curves would be useful to model possible progenitor populations, and to compare our results with those of other low frequency surveys. This is the case for many FRB studies to date (Petroff et al. 2015).

3.1 Beam Model

The beam model is an approximation of the direction dependent sensitivity, across the field of view, of the array. Thus, correcting for this differential gain response pattern ensures that the light curves of detected sources are flat, as they move across the field of view.

This pattern is the result of many physical factors including: observing frequency, the geometry of the stations and dipoles, their mutual interactions with each other, and

Parameter	AARTFAAC LBA	Comment
Array elements	288 inverted V antennas	Dual polarized elements
Frequency range	10-90 (MHz)	
Field of view	π (sr)	FWHM of beam
Total Effective area	2617 ^a (m ²)	
T_{sys}	3600 ($\nu^{-2.55}\text{K}$)	
Angular resolution	60 (arcmin)	
Subband resolution	195 (kHz)	
Processed Bandwidth	3.12 (MHz)	
Temporal resolution	1 (s)	

Table 2. AARTFAAC system design specifications, from Table 1 of (Prasad et al. 2014). Here the subband and processed bandwidth values are updated to reflect the current operational capabilities of AARTFAAC.

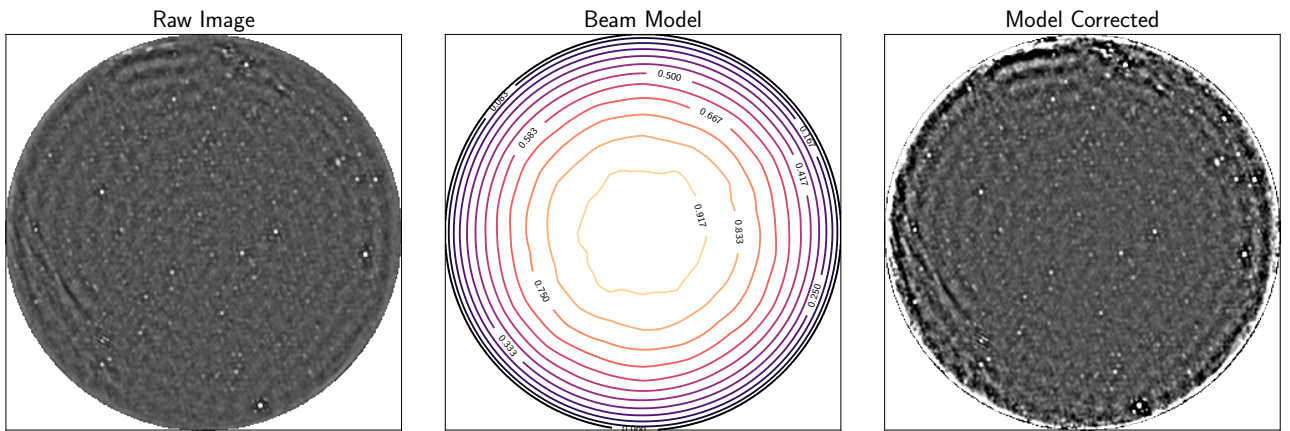


Figure 1. Left: An AARTFAAC all-sky image, output by the imaging pipeline, after A-team subtraction. Centre: A normalized beam model, for AARTFAAC at 60MHz. The model shows the shape of the direction dependent gain across the field of view with maximum gain at zenith, decreasing toward the horizon. Right: the same image with the correction applied. Note, these images have not been flux density calibrated so the pixel scaling is arbitrary.

the effect of the local terrain. Given these complicated interactions, it is modelled by simulating the full station layout of all of the dipoles which form the six stations on the LOFAR Superterp, with accurate placement and orientation, across the frequency spectrum.

Therefore, the beam response shape has been modelled at frequencies between 30 and 70 MHz in 5 MHz intervals. This covers the spectral range of AARTFAAC with sufficient accuracy, since the model does not change rapidly with frequency. These models were generated using WIPL-D, an electromagnetic simulation software package. Additionally, Fig. 2 illustrates the symmetry of the model at 60 MHz, about the zenith.

The left image of Fig. 1 shows an example raw AARTFAAC image. Although the background and noise appear flat across the image, sources decrease in apparent brightness as the sensitivity drops toward the horizons. The sensitivity peaks at zenith and decreases toward the horizon. Therefore the images are corrected by dividing the raw image by the image of the beam model, normalized such that the gain at zenith is 1. The shape of the normalized beam model at 60 MHz is illustrated in the middle panel of Fig. 1, and the resulting beam corrected image is shown on the right. Given that the sensitivity near the horizon is lower,

after the correction is applied, the noise near the horizon is also multiplied. However, the mean flux density of sources will be constant as they rotate through the beam, as illustrated in Fig. 3.

Although the beam model has been observationally verified during LOFAR commissioning (van Haarlem et al. 2013), AARTFAAC is able to perform an additional test, using sources detected across the field of view, observed over hours as they move across the sky. After calibrating the data, the extracting flux measurements of each source at different locations on the sky were compared to the mean of their light curve. No position dependent deviations, which would indicate an improperly modelled beam, were observed within our detection region of 50 degrees from zenith.

3.2 Reference Catalogues

Given the real-time streaming nature of AARTFAAC observations, an algorithm that computes the flux scaling per image, using only the image itself, is preferred. This excludes traditional flux density scale calibration techniques, such as intermittently observing another field with a calibrator source.

Fortunately, with our field of view encompassing the

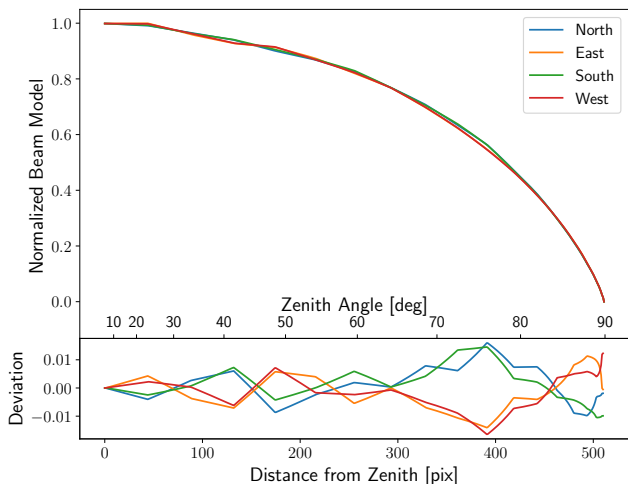


Figure 2. Comparing the beam model gain pattern at 60 MHz, from zenith to horizon, in the four compass directions. The values are normalized to their maximum value, which is at zenith. The beam is highly symmetric about the zenith, with relative deviations from perfect symmetry below 1% out to 70°.

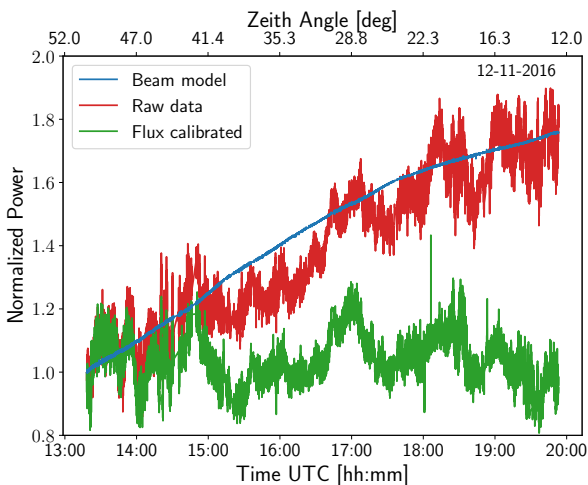


Figure 3. Example light curve for a source observed for ~ 7 hours, normalized to the first data point. The raw data (red) before calibration clearly shows the shape of beam pattern along the track of the source across the sky (blue), while after calibration (green) the curve is much flatter.

entire sky, enough bright sources are present in each image to compute the scaling in real-time. However, this is only possible if accurate apparent fluxes at the observing frequency are known. Therefore, with a population of enough bright sources covering the Northern Hemisphere, the apparent brightness of those sources extracted in each image can be compared with the expected flux density, and the conversion scale factor computed. This is described fully in Section 3.3.

Furthermore, utilizing the greatest number of calibra-

tors ensures that the variability of any one source does not dominate the calibration solution. Additionally, ionospheric fluctuations are phenomena localized on the sky, as density fluctuations travel through the field of view, and therefore decorrelate on larger angular sizes. To this end, gathering together a catalogue of all sources with a signal-to-noise ratio $> 5\sigma$, and broadband spectra across our entire observing range, and field of view, would allow accurate and stable flux density calibration at any observing frequency.

Recently, several catalogues of calibrator sources have been published with accurate broadband spectra in the LO-FAR LBA range, 30-80 MHz:

One example, Scaife & Heald (2012) contains six bright sources from the Third Cambridge Catalogue, 3C, with spectral models between 30 and 300 MHz. Unfortunately, with only six sources spanning the Northern Hemisphere, AARTFAAC images would not contain enough calibrator sources to ensure a robust scaling solution at all observing times. However, the analytic spectral models across the full LBA band and the fact that these sources appear in the other catalogues adds a useful inter-catalogue check.

Secondly, Perley & Butler (2017) published modelled spectra for 20 sources with flux density measurements down to 74 MHz. Four of these are the A-team sources which are subtracted from the images before this flux density calibration step, leaving 16 sources. Of these, 6 have a declination $< -10^\circ$, and are therefore outside, or too near the edge, of our field of view. This leaves 8 sources which are viable flux density calibrators. Even still, rarely are more than 3 of these sources visible in the sky simultaneously, which is preferred to have stable flux density fit solution at all times.

Lastly, the catalogue published by Helmboldt et al. (2008) contains spectra for 388 sources selected from VLSSr which are brighter than 15 Jy at 74 MHz. The spectral shapes of all sources are described with either a single power-law, or if enough data are present, by the function $Y = A + BX + C \exp(DX)$, where $Y = \log(F_\nu/1 \text{ Jy})$ and $X = \log(\nu/74 \text{ MHz})$, which describes a spectral turnover of the flux density, F_ν , at lower frequencies, ν , in some sources.

In addition to these, the full VLSSr catalogue (Lane et al. 2014) was used to follow up sources which are detected in AARTFAAC images with $> 5\sigma$ signal-to-noise but are not associated with any object in the Helmboldt et al. (2008) catalogue. These might result from two or more sources in VLSSr with $< 15 \text{ Jy}$ that are sufficiently close together to be confused at AARTFAAC’s resolution.

The lower resolution of AARTFAAC and the densely packed array allows us to see much more diffuse emission than the VLSSr. For this reason, the supernova remnant catalogue by Green (2014) was also used for source association. These objects are of interest to us because they are bright at low frequencies, and their larger angular size reduces the effect of ionospheric scintillation. However, due to the frequency at which these flux densities are given (1.4GHz) and the much narrower beam width, it is impossible to simply extrapolate and compare with AARTFAAC measurements.

The spectral models published by Perley & Butler (2017) are much more accurate in the frequency range observed with AARTFAAC. However, this catalogue does not contain enough sources across the Northern Hemisphere to ensure that 3 or more sources are observable simultaneously, which is a requirement, used to ensure a more stable scaling

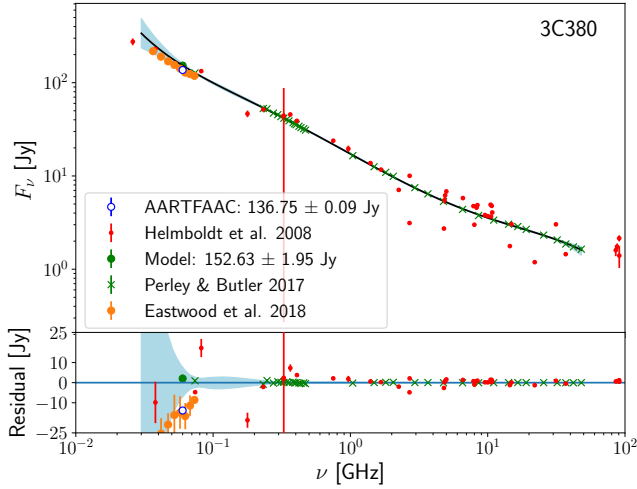


Figure 4. The spectral model of 3C380 is generated from the flux density measurements by Perley & Butler (2017). The uncertainty in the model (light blue region) is calculated via Monte Carlo random sampling of sets of measurements based on their reported uncertainty. This gives the model value at our measurement frequency, 60 MHz (green filled circle). The AARTFAAC catalogue flux density value (open circle) and Helmboldt et al. (2008) measurements (red dots) and Eastwood et al. (2018) measurements (orange filled circles) are compared to the model (black line). The residuals show the difference between the measured values and the model.

solution in the presence of scintillation. And while Helmboldt et al. (2008) present a catalogue with many more sources, the simpler spectral models result in a much greater uncertainty in the flux density predictions below 74 MHz. Neither catalogue was therefore sufficient to accurately compute a flux density scale at all times. This necessitated the creation of the AARTFAAC low frequency catalogue, which is outlined in detail in Section 5.

3.3 Flux density scale

The AARTFAAC catalogue was created by first modeling the Perley & Butler (2017) source fluxes at lower frequencies. This was done by using a Monte Carlo method where 10,000 sets of flux density measurements for a given source at different frequencies were generated using the flux density measurements and uncertainties available in the supplementary online data. Next a least squares fit was done to the spectral models with the same polynomial degrees as those in Perley & Butler (2017):

$$\log(F_\nu) = a_0 + a_1 \log(\nu_G) + a_2 \log(\nu_G)^2 + a_3 \log(\nu_G)^3 + \dots \quad (1)$$

where F_ν is the flux density in Jy and ν_G is the frequency in GHz. Finally, the resulting functions are then evaluated at the AARTFAAC observing frequency. This provides predicted fluxes with accurate uncertainties. The spectral model for one such source, 3C380, is shown in Fig. 4, along with the flux density measurements from Helmboldt et al. (2008) and Perley & Butler (2017). Here, the model predicted flux density at 60 MHz, and the final AARTFAAC catalogue flux density, after averaging the data from all observations, is

shown not to be in agreement, within their mutual uncertainties. However, when comparing with the flux density as measured by Eastwood et al. (2018), the differences are much smaller for all sources, except 3C286. Therefore, because of the similarity of the LOFAR-LBA and OVRO-LWA antenna design, but different imaging and calibration method, it is clear that the measured flux density at 60 MHz is accurate.

The AARTFAAC catalogue is then made by bootstrapping the flux density scale from these sources in the following way:

First, an observation of a few hours was considered at a time when 5 calibrator sources were visible.

Then the predicted flux density values at 60 MHz, obtained from the reference catalogue, were compared to their sigma-clipped light curves extracted from the observation. Iteratively clipping the flux density measurements greater than 3σ from the mean reduces the possible effect of RFI or imaging artifacts.

Light curves are generated by extracting the source fluxes from each image with the Python Source Extractor (Carbone et al. 2018), then the sources extracted from each image are associated with the extractions from previous images in a running catalogue database. This is performed using the LOFAR Transient Pipeline (TraP; Swinbank et al. 2015, and references therein).

The durations of the observations used for generating the catalogue were each longer than 2 hours. This ensures that scintillation effects shown in Fig. 3, which occur on a 15-20 minute time scale (Loi et al. 2015b), are averaged out.

We then calculate the scaling solution via linear regression, weighting the sources according to their measurement uncertainty. The single scale factor calculated for that observation was then applied to the mode of the flux density measurements of the other persistent sources, detected above 5σ .

Those inferred values and our measurement of the original reference sources are added to the AARTFAAC catalogue. By adding the additional calibrators, and using the new AARTFAAC catalogue as a reference for the other observations where fewer Perley & Butler (2017) calibrators are visible, a more accurate scale factor for each additional observation can be calculated.

To summarize, in each new observation, all light curves longer than 2 hours are extracted, the scale factor for the observation is calculated, and it is applied to the new sources, then the new sources are added to the catalogue. The number of data points for each source is recorded so that when a source, which already exists in the catalogue, is re-observed, a mean weighted by the number of measurements is used to calculate the updated flux density value.

Now that the entire Northern Hemisphere has been observed, and all persistent sources detectable above 5σ , flux densities of 40-50 Jy for much of the sky, have been added, the AARTFAAC catalogue can be used to flux density calibrate any individual AARTFAAC image. This is possible because there are 30-50 observable sources above this threshold at any time. This greater number of sources, across the full field of view, provides a stable flux density solution.

Finally, the AARTFAAC catalogue was used to correct the flux density scale on the full 33 hours of data. This was done in a streaming mode, calculating the the linear scaling solution for each image independently, so that the in-

tended use case could be analyzed by verifying light curves extracted from the data. In doing so we observed that the scaling solution did have a dependence on LST, which was expected due to the scaling of the raw visibilities according to the total power of objects in the field of view, but that the scaling solutions, at a given LST, were stable across the months spanned by the set of observations.

4 ANALYSIS OF FLUX CALIBRATED DATA

AARTFAAC produces a snapshot image of the entire sky at a rate of 1 per second. To this stream of images a correction for the antenna response pattern, as well as a scale factor, per image, is applied. This enables the creation of a reliable light curve for each source. In the previous section, the method for correcting each image by applying the beam model and calculating the scale factor, required to scale the pixel values to flux densities in janskys, was discussed.

Each of these corrections influence the light curves on different time scales: the varying sensitivity of the antenna will modulate the apparent brightness over a long period of time as the source moves across the sky, whereas the flux density scaling is corrected on each image independently and would therefore have its effect on the timescale of ionospheric fluctuations.

Turbulence in the ionosphere causes the apparent brightness, as well as the position and shape, of sources to fluctuate. This reduces the instantaneous accuracy of measurements from individual AARTFAAC images. Fortunately, this is overcome by observing each source for a sufficiently long time that the mean value of the light curve converges.

The length of time for which each source must be observed depends in general on the typical timescale of ionospheric scintillation. For example, if a source is observed many times, but for a shorter duration than the timescale of these fluctuations, the variance of the light curves, and thus the uncertainty in the flux density will be dominated by the ionospheric fluctuations.

As an example Fig. 5 illustrates this for the Tycho supernova remnant. Large sources of synchrotron emission, such as supernova remnants generally do not intrinsically vary in brightness, making them useful tools to study the systematic effects on our flux density measurements.

For a pure Gaussian noise process the standard error in the mean, SEM, defined as the standard deviation of the means calculated from subsets of the data, decreases proportional to the number of samples in the subset, $\sigma_{m,N} \propto N^{-1/2}$. This is the green ‘‘Theoretical’’ line in Fig. 5a, scaled by the average uncertainty in each individual integrated flux density measurement, Δf_{int} .

However, Fig. 5d illustrates that AARTFAAC flux density measurements are not a pure Gaussian process. In fact, despite the larger angular size of Tycho, its light curve, shown in Fig. 5c, reveals that the measured flux density is still significantly modulated by the ionosphere.

There are therefore two regimes, timescales much less than, or much greater than the timescale of ionospheric fluctuations, $10^2 - 10^3$ seconds, which represent the dominant sources of uncertainty in AARTFAAC flux density measurements.

First, the statistical uncertainty in each individual source fit due to the image noise. For timescales much less than the fluctuations in the ionosphere ($<10^2$ seconds), these measurements are highly correlated and thus not independent. This is due to the fact that AARTFAAC images are confusion noise limited. The noise profile is therefore below what is estimated by the individual source fits. This is evident in the left side of Fig. 5a, where the ‘‘Sequential sample’’ curve, generated by calculating the mode of subsamples from the light curve sequentially over increasing time, is below the pure Gaussian estimate.

Secondly, the variation of the brightness due to the electron density fluctuations in the ionosphere. Again, the noise profile differs from the Gaussian estimate for light curves much longer than the typical ionospheric timescale ($>\sim 10^2$ seconds). The variation caused by the ionosphere causes fluctuations which are greater than the estimated uncertainties from each image. This effect causes the estimated error to cross above the Gaussian estimate.

Furthermore, observing a source for many hours will result in significant motion across the sky, and through the beam of the antenna. Fig. 3 illustrates an example of correcting for the antenna response on a source, whose light curves have been normalized to the first data point. Clearly, in the raw light curve (red) the increasing sensitivity of the antenna is visible as the source rises in the sky toward zenith. Along side this, the beam response pattern along the path of the source (blue) illustrates how as the sensitivity increase toward zenith and the beam centre, explaining the dramatic increase in the apparent brightness. When the beam model is divided out, a much flatter calibrated light curve (green) remains. In fact, the residual variability in the light curve shown is predominantly due to turbulence in the ionosphere, causing the apparent brightness fluctuations.

Consequently, these noise characteristics indicate that observations shorter than a few minutes duration, may not yield an accurate average flux density value, regardless of the noise properties in each individual image. However, the histogram of flux density values measured from the entire observation, shown in Fig. 5d, illustrates that the noise profile is, by appearance, nearly Gaussian, after observing the source for a period significantly longer than the timescale of the ionosphere. This is to be expected given the central limit theorem. Therefore, making prolonged observations results in both accurate and precise flux density measurements.

4.1 Flux density measurement statistics

As the noise was expected to be Gaussian, with potential systematic influences from either the ionosphere or an incorrectly modelled beam pattern, a skewed normal Gaussian distribution was fit to each light curve.

$$f(x) = \frac{2}{\omega} \phi\left(\frac{x-\xi}{\omega}\right) \Phi\left(\alpha\left(\frac{x-\xi}{\omega}\right)\right), \quad (2)$$

where ϕ is the standard normal probability distribution and Φ is its cumulative distribution, and the transformation $x \rightarrow \frac{x-\xi}{\omega}$, to the fitted parameters ξ , the location, ω the scale, and α , the shape, which defines skewness. The skewness increases with the absolute value of α , with more weight in the left tail when $\alpha < 0$ and in the right tail when $\alpha > 0$, when $\alpha = 0$ the skewed normal distribution becomes the

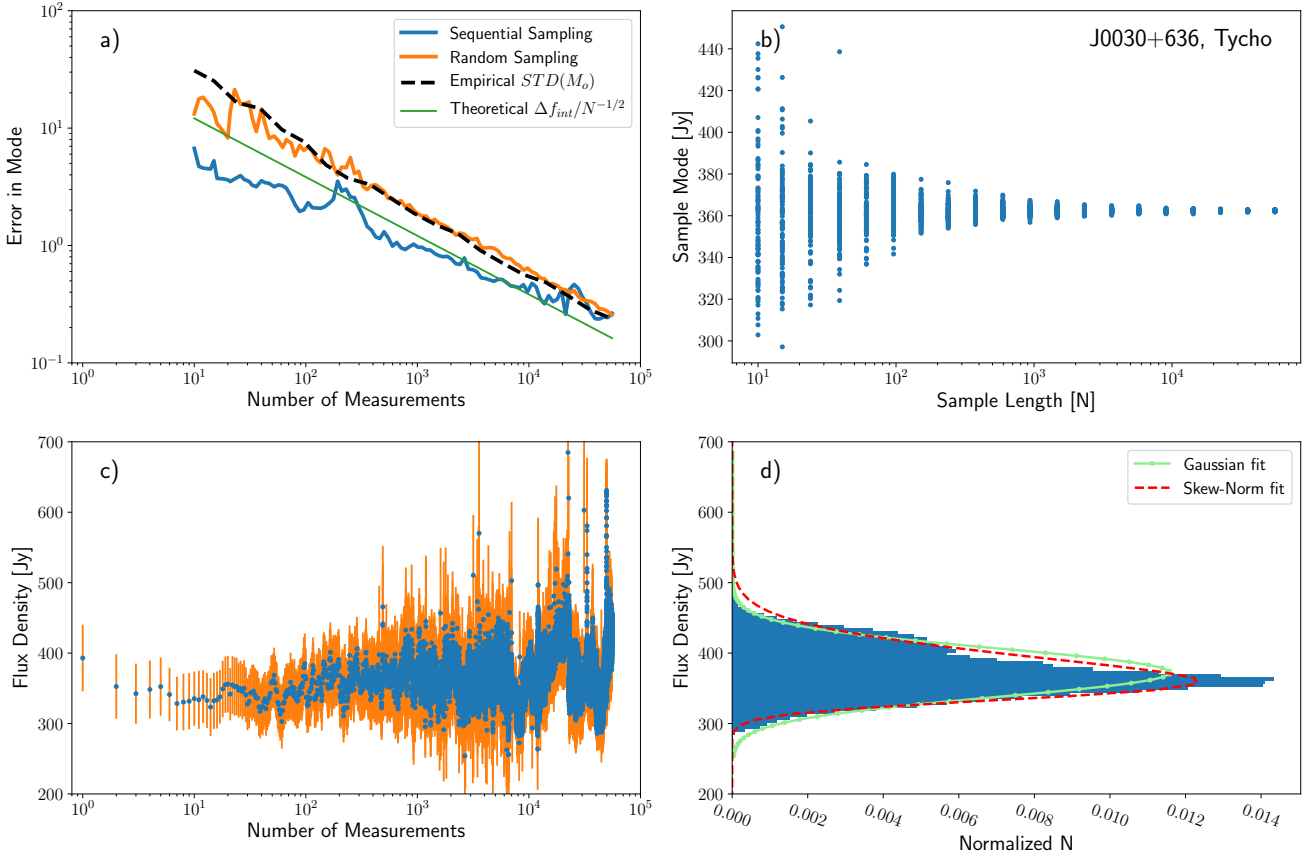


Figure 5. The noise profile of the Tycho supernova remnant. The source is intrinsically stable due to its large size, and emission mechanism, so fluctuations in its measured flux density are due strictly to either source fit statistics or ionospheric fluctuations. Figure a shows the error in the mode as a function of sample size, for different methods of sampling the data, and different methods of estimating the uncertainty. The sequential sampling curve (blue) was generated by taking subsets of the measurements from the light curve in order. This shows how the uncertainty is affected by the systematic sources of error over time. The random sampling curve (orange) was generated by randomly sampling, with replacement, from the entire light curve and estimating the uncertainty in the mode of that subsample. The empirical (black dashed) was calculated by randomly sampling multiple subsets of the light curve, then calculating the standard deviation in the modes of those subsets, then repeating this for a number of sample lengths. These populations of mode, from different subsets, are plotted in figure b. Lastly the theoretical line (green) shows how the standard error in the mean value of the data would be expected if the noise were purely Gaussian, independent and equal to the average uncertainty in the fit from each image. Figure c shows the entire light curve of Tycho from our set of observations, with the uncertainty of each measurement in orange. Lastly, figure d presents a histogram of the data, and a comparison to a normal and skew normal distribution.

normal distribution, and ξ is simply the mean, and ω the standard deviation.

After fitting Eqn. 2 to each of the light curves, it was found that the skewness was most frequently positive, with a larger tail in the distribution towards higher flux. This could indicate that the variation, introduced by the ionosphere, preferentially focuses the light into shorter bright caustics. These move along the ground, similar to the light on the bottom of a swimming pool.

Consequently, simply integrating over long observations, either by simple average, or calculating the median would yield results biased by the preference for outliers with increased brightness. Hence, the mode of the distribution is the most robust measurement of the central tendency of each source, and therefore the most accurate description of its flux density.

However, the mode of the skew normal distribution is not analytic, but can be approximated numerically,

$$M_o \approx \xi + \omega m_o(\alpha), \quad (3)$$

where the ξ , ω , and α , are the fit parameters location, scale, and shape, of the distribution. The function $m_o(\alpha)$ is the degree to which the skew modifies the mode from the mean, which for a normal distribution is equal to 0. This is given by,

$$m_o(\alpha) \approx \mu_z - \frac{\gamma_1 \sigma_z}{2} - \frac{\text{sgn}(\alpha)}{2} \exp\left(-\frac{2\pi}{|\alpha|}\right). \quad (4)$$

where $\sigma_z = \sqrt{1 - \mu_z^2}$, such that

$$\mu_z = \sqrt{\frac{2}{\pi}} \delta,$$

for

$$\delta = \frac{\alpha}{\sqrt{1 + \alpha^2}},$$

and where γ_1 is the skewness,

$$\gamma_1 = \frac{4 - \pi}{2} \frac{(\delta\sqrt{2/\pi})^3}{(1 - 2\delta^2/\pi)^{3/2}} \quad (5)$$

The parameters were fit using the Bayesian inference MCMC package PyMC3. This method randomly samples the parameters from defined prior distributions, then computes the likelihood. The uncertainty estimate was output by the PyMC3 package (Salvatier et al. 2015). By defining the mode as a deterministic function of the fit parameters, PyMC3 gives the resulting uncertainty of the mode directly, as well as producing a covariance matrix for the parameters, and plots of the marginal posterior probability distributions.

The robustness of the mode and correctness of the uncertainty calculation was tested in two ways.

First, subsets of the data of varying length were randomly sampled with replacement, from the light curve. Then the mode of each subset was calculated. Fig. 5b shows the variance in the mode of each sample of Tycho flux density measurements, taken from different length intervals of the total observation. As the length of these intervals was increased, the standard deviation of the mode of each subset was calculated, and plotted as the dashed black line in Fig. 5a.

Then, the ‘‘Random Sampling’’ curve in Fig. 5a shows the estimation of the uncertainty in the mode of a randomly drawn sample from the light curve. Comparing these uncertainty estimates, the PyMC3 estimate from the random sample, with the empirically measured standard deviation of the modes from a number of different subsets, and the estimate calculated from the fit parameter uncertainties added in quadrature, provides an additional independent verification of the reported uncertainty.

As previously argued this catalogue presents the mode of the skew normal distribution as the most robust measurement of the flux density of each source, under the influence of a turbulent ionosphere. The observed tendency toward positive skewness indicates that longer integrations, or simply averaging successive shorter integrations, would yield a positive bias in the inferred flux density.

Given that AARTFAAC images are generated and calibrated at a rate of one per second, well below the typical time scale of ionospheric scintillation, it is possible to observe a large number of flux density measurements, fit the distribution, and calculate the mode. However, other low frequency surveys typically make much longer integrations to reduce the image noise level. Therefore the quantity which should be compared is the mean, rather than the mode. The mean, μ , of the distributions fit can be calculated from the parameters given in the catalogue as follows,

$$\mu = \xi + \omega\delta\sqrt{\frac{2}{\pi}}. \quad (6)$$

Lastly, the uncertainty presented in the flux densities are the statistical uncertainty in the modes of each distribution. As shown in Fig. 5a follow up measurements would agree within the stated uncertainty if the duration of the observations is sufficient. However, observations shorter than

the ionospheric time scale could only be expected to agree within the standard deviation, described by,

$$\sigma = \sqrt{\omega^2 \left(1 - \frac{2\delta^2}{\pi}\right)}. \quad (7)$$

5 CATALOGUE

5.1 General properties

The aim of this catalogue is to fill the gap between the VLSSr at 74 MHz (Lane et al. 2014) and the 8C catalogue at 38 MHz. Indeed, for many sources below the 60° degree declination limit of the 8C survey, this catalogue contains the lowest frequency flux density measurement. The source detection region extends to 50° from zenith. As a result of correcting the effect of the primary beam, the background noise increases from zenith toward the horizon. However, within 50° from zenith the noise is roughly constant or increases slowly. Beyond 50° however, the background noise is greater than twice the noise at zenith and increases dramatically. Given that zenith is toward 52.9° declination at the LOFAR superterp, the survey covers the full Northern Hemisphere. This is illustrated in Fig. 6, where the coverage area of the AARTFAAC catalogue is compared to the Perley & Butler (2017), Helmboldt et al. (2008), and the 8C (Rees 1990) catalogues.

This catalogue will also be beneficial as an independent check for the calibration of low frequency, wide field images generated by the LWA and other LOFAR-LBA surveys such as the forthcoming MSSS. Additionally, the technique presented here can be implemented for real-time streaming calibration of the Southern Hemisphere arrays MWA and SKA-LOW.

5.2 Position

The uncertainties in the position measurements by AARTFAAC are large relative to other surveys due to the lower resolution of the images. Fortunately, given the threshold to which we detect sources, the resulting number density in the sky is such that this does not cause a problem when associating measurements of any source across the set of images in an observation. Correspondingly, within an association radius of 1° any AARTFAAC source can be uniquely matched. Moreover, since the primary goal is the creation of a catalogue for flux density calibration to compare with future transients, highly accurate source positions are not essential.

Nevertheless, the best estimate of the position of each source was measured. This was done by taking the mean, weighted by the uncertainty in the fitted position from each extraction.

5.3 Reference source fit

The accuracy with which the fluxes of the modelled reference sources are measured from the images, after calibration, is a validation of the models. This is due to the fact that, as more sources are added to the catalogue and incorporated into the calibration scheme, the inferred flux density of a

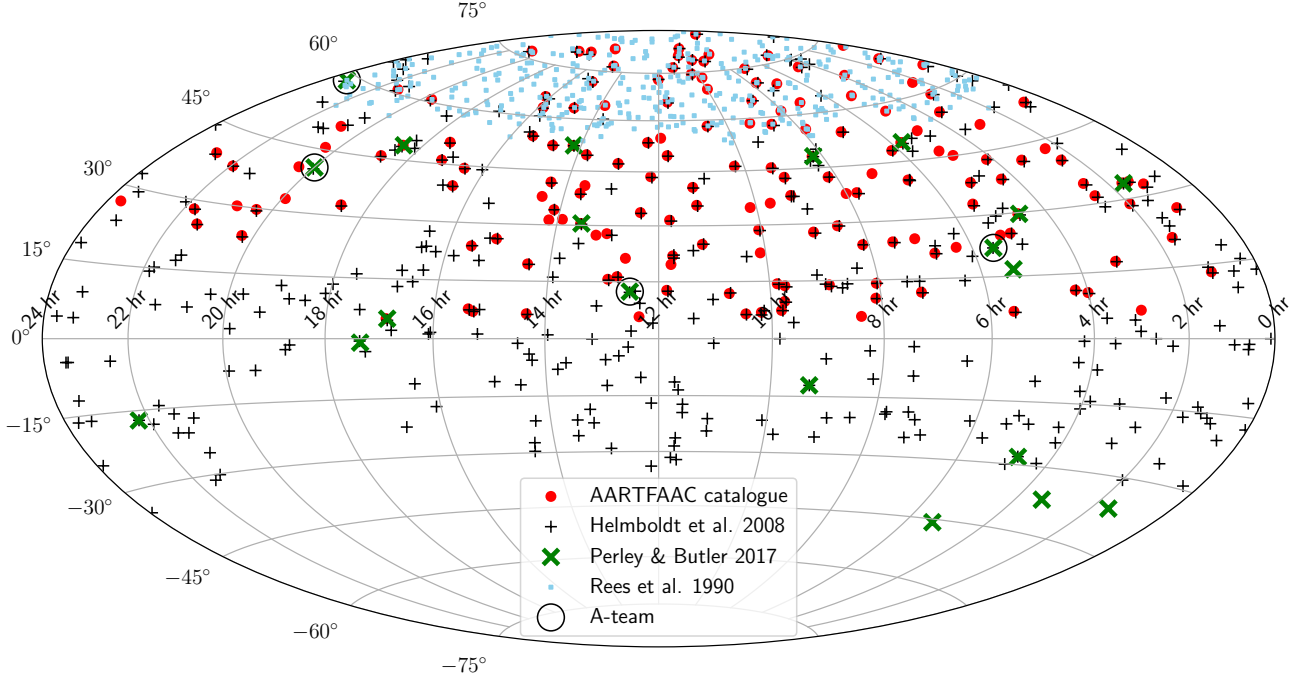


Figure 6. A comparison of the 167 AARTFAAC catalogue sources, and the primary reference sources: 23 in [Perley & Butler \(2017\)](#) of which 8 are observable above a declination of 0° , and 388 from [Helmboldt et al. \(2008\)](#) of which 120 are associated with AARTFAAC sources.

Source Name	Scaife and Heald Model [Jy] @ 60 MHz	Perley and Butler Model [Jy] @ 60 MHz	AARTFAAC Measured [Jy] @ 60 MHz	Eastwood et al. Interpolated [Jy] @ 60 MHz
3C48	77 ± 5	74.55 ± 0.64	81.36 ± 0.33	83.7 ± 2.29
3C123	-	473.75 ± 3.87	462.85 ± 0.33	-
3C147	43 ± 4	50.59 ± 0.66	48.71 ± 0.14	44.89 ± 1.02
3C196	151 ± 5	151.84 ± 1.25	157.30 ± 0.20	-
3C286	33 ± 2	29.15 ± 0.25	47.69 ± 0.12	32.63 ± 0.43
3C295	134 ± 11	138.65 ± 1.13	112.55 ± 0.18	125.22 ± 3.44
3C380	156 ± 4	152.63 ± 1.95	136.75 ± 0.09	134.49 ± 3.70
Hercules A	-	876.31 ± 10.55	873.07 ± 0.37	-

Table 3. A comparison of the difference between the AARTFAAC inferred flux density, and values modelled from the spectral fits presented in the reference catalogues. The modelled flux density, and associated uncertainties, for the [Perley & Butler \(2017\)](#) catalogue were generated via a Monte Carlo method, by fitting a spectrum to random samples of the flux density measurements. These values were used as the initial flux density scale for bootstrapping to the entire AARTFAAC catalogue. Additionally for comparison, the modelled flux density from [Scaife & Heald \(2012\)](#) are shown. These flux density estimates, and uncertainties, were generated using the coefficients and their uncertainty in the spectral model published. As such, the uncertainty in these flux density estimates at 60 MHz is much higher. Lastly, the our values are compared to the results of [Eastwood et al. \(2018\)](#), interpolated to 60 MHz.

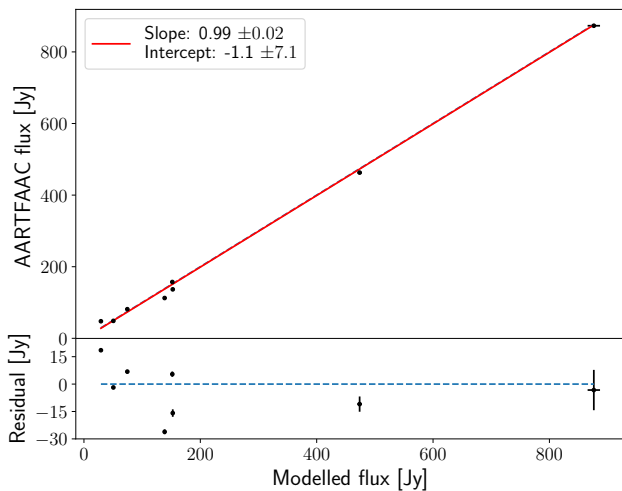


Figure 7. Comparing the modelled flux density of the initial calibrators, from [Perley & Butler \(2017\)](#) to their AARTFAAC measured flux density. This shows excellent relative brightness agreement across the sources. The exception is the faintest source 3C286, with a modelled flux density of 29.15 ± 0.25 Jy and a measured flux density of 47.69 ± 0.12 Jy. Measurements reported by [Helmboldt et al. \(2008\)](#) also have a large scatter around the model across the frequency range. This may be due to systematic differences among the different surveys.

single incorrectly modelled source would diverge from the initial estimate, due to the influence of the other correctly modelled sources on the flux density scaling fit for the entire image.

In order to illustrate the resulting goodness of fit between the modelled reference fluxes used in calibration and the resulting measurements, the spectrum from [Perley & Butler \(2017\)](#), with our AARTFAAC data point (open circle), is shown in Fig. 4. Here, the AARTFAAC measured flux density does not agree, within the uncertainty of the reference model (blue region). In fact, Fig. 7 and Table 3 show that the only source for which the reference model and AARTFAAC measurement agree within their combined uncertainty is Hercules A, the brightest source.

However, a strong linear relationship between the reference flux density and the measured flux density, is illustrated in Fig. 7. This illustrates the linear response of the array to sources from 50 to over 800 Jy. And suggests that the relative brightnesses of the models are not completely accurate at 60 MHz.

Lastly, our flux density values were compared to those measured by the Owens Valley Long Wavelength Array (OVRO-LWA), ([Eastwood et al. 2018](#)). The OVRO-LWA flux density values compared in Table 3 are derived by interpolating between the measured values, provided in their supplementary online material, and the uncertainties calculated using a Monte Carlo method to randomly draw a population of flux density measurements within the reported uncertainty range. Notably, the sources 3C48 and 3C380 both agree within mutual uncertainties. This is interesting due to the similarity of the instruments, but very different method for calibration and imaging.

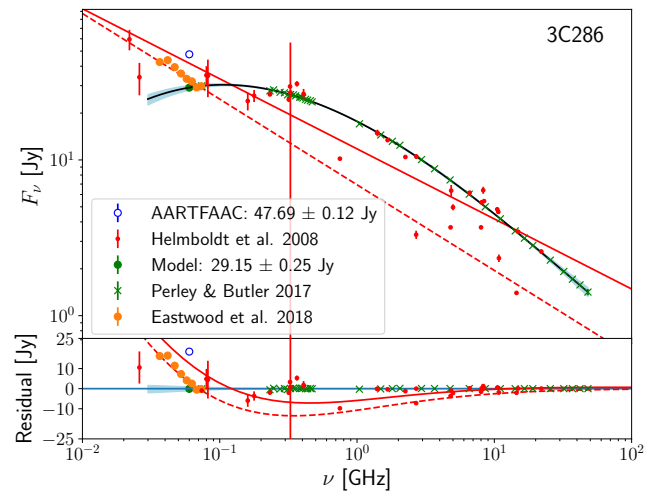


Figure 8. A comparison of the collected reference measurements of the flux density of 3C286, compared to the AARTFAAC measurements (open circle). The [Perley & Butler \(2017\)](#) measurements (green x's) and modelled spectra (black line) was used for the initial catalogue bootstrapping. While values reported by [Eastwood et al. \(2018\)](#) (orange circle) are direct measurements at frequencies comparable to AARTFAAC with the OVRO-LWA, an instrument with a similar design to AARTFAAC. However the flux densities reported by [Helmboldt et al. \(2008\)](#) (red dots) show the high variance in published flux densities across the spectrum. Two simple power-laws (solid and dashed red lines) fit by [Helmboldt et al. \(2008\)](#) are also shown. Interestingly both AARTFAAC and OVRO-LWA agree better with the simple power-laws shown here.

Lastly, it is apparent that the flux density measured here for 3C286 is significantly higher than what is reported by all three of the reference catalogues. It is unclear what could cause this for a single source. 3C286 is a very well known calibrator. In an attempt to explain the additional flux, measurements by a single dish instrument, in which 3C286 is unresolved ([Ott et al. 1994](#)) were compared. However, this study yielded results that agree with the measurements of [Perley & Butler \(2017\)](#) using the VLA, indicating that we are not observing additional diffuse flux as in the case of the Tycho supernova remnant. Additionally, given that 3C286 is at a high Galactic latitude, 10° north of the North Galactic Spur, it is unlike likely the additional flux is the result of diffuse Galactic emission removed by simply imposing the minimum baseline of 10λ . Further, there is no correlation between sky location and deviations between the modelled and measured flux densities. When viewing the AARTFAAC measured flux density alongside the flux density values and simple spectra reported by [Helmboldt et al. \(2008\)](#), illustrated in Fig. 8, the difference does not appear as anomalous. In fact the power-law spectra fit by [Helmboldt et al. \(2008\)](#) predict a flux density at 60 MHz of 42 Jy. While these data and spectra are less precise than those measured by [Perley & Butler \(2017\)](#), it is notable that both the results from AARTFAAC and the OVRO-LWA are better predicted by these spectra.

AARTFAAC Label		VLSSr Label
J0110+322	-	J0110+315
J1011+068	-	J1011+062
J1147+496	-	J1146+495
J1445+768	-	J1447+766
J1630+442	-	J1629+442

Table 4. A list of sources for which a spectral turnover was predicted, which we do not observe. Here the signifier from the AARTFAAC and VLSSr are given. In the supplemental online material the AARTFAAC flux density measurements are compared alongside the measurements and spectral fits in figure 1 of [Helmholtz et al. \(2008\)](#).

5.4 Spectral turnovers

Some of the spectral models fit by [Helmholtz et al. \(2008\)](#) predict a turnover below the lowest frequency at which measurements were made. Nevertheless, the new flux density measurements made at 60 MHz clearly indicate that, instead, the spectral shape of at least six of these sources continue to rise. The spectra for the six sources, whose labels from both the AARTFAAC catalogue and VLSSr catalogue are listed in Table 4, can be seen in the supplemental online material, where the AARTFAAC measurement is plotted alongside the flux density measurements and spectral fits from [Helmholtz et al. \(2008\)](#). An example of these figures is shown in Fig. 9, where the flux density measurements from [Klein et al. \(1979\)](#) are plotted as well.

Further ongoing flux density studies, across the full observational spectrum of the LOFAR LBA, 10-90 MHz, could potentially reveal turnovers at a frequency lower than 60 MHz.

5.5 Blended sources

One issue with interferometers is that the minimum baseline length determines the sensitivity of the instrument to regions with large diffuse emission. Therefore, objects with a larger angular size will have their diffuse emission, at least partially, resolved out by interferometers which achieve a high angular resolution. This reduces the total apparent flux density of diffuse sources when compared to measurements by a single dish instrument. Consequently, in order to remove the large, bright, diffuse structure of the Milky Way we eliminate all baselines below 10λ . This effectively eliminates much of the Galactic emission which would otherwise be a dominant foreground.

In observing large diffuse sources, such as nearby supernova remnants, we see that AARTFAAC recovers the total integrated flux density as effectively as a single dish instrument. This effect is shown in Fig. 9 for the supernova remnant Tycho, where the flux density measurements (red dots) and spectral fit (red line) reported by [Helmholtz et al. \(2008\)](#) are compared with a multi-wavelength analysis observed with a single dish instrument by [Klein et al. \(1979\)](#) (blue circles). Additionally, the integrated flux density value from the 8C catalogue is plotted in green. Consequently, the sensitivity of AARTFAAC on larger angular scales presents an additional use case beyond

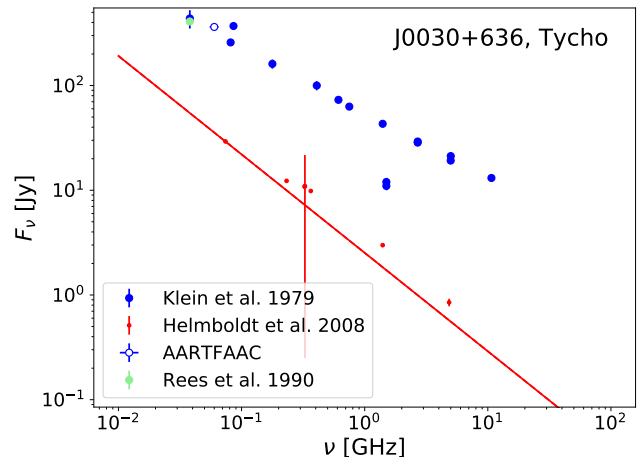


Figure 9. The spectra of the supernova remnant 1572, also known as Tycho. The measurements reported by [Helmholtz et al. \(2008\)](#) (red dots) show a significantly reduced integrated flux density compared to the AARTFAAC measurement at 60 MHz. This is due to the higher resolution of these surveys resolving out power in the diffuse emission. Comparing this to the multi-frequency single dish measurements by [Klein et al. \(1979\)](#) (blue circles), the 8C catalogue ([Rees 1990](#)) (green circle), and AARTFAAC (open circle) which fully recover flux density on this scale like a single dish instrument, as a result of their lower resolution.

transients; for example, to study Galactic emission, and diffuse regions around other sources such as Cassiopeia A and Cygnus A.

Due to the relatively low resolution of AARTFAAC, compared to the 8C and VLSSr surveys, some objects reported here as individual sources are known to be composed of two or more sources blended together. By comparing the AARTFAAC catalogue to VLSSr with integrated flux density greater than 10 Jy we find that the sources listed in Table 5 are the result of multiple blended objects.

However, so long as the sum of these blended sources maintains a stable flux density the component contribution of each is not important for us, since AARTFAAC does not resolve them independently. Therefore, no effort was made to de-blend the sources, and attempt to retrieve an accurate flux density for each individually. The blended sources, as they appear to AARTFAAC, are still useful for our calibration purposes. Although instruments with a higher resolution, including AARTFAAC after the currently planned extension which will incorporate 6 additional stations, may need to exclude these when calibrating, and measure the separate component fluxes.

5.6 Summary of flux calibration and measurement accuracy

From all the above, it is clear that a number of significant factors play a role in the accuracy with which AARTFAAC can report calibrated source fluxes: the stability and sensitivity of our instrument, the stability of the ionosphere, and the ability to relate our instrumental brightness measure-

AARTFAAC Label	VLSSr fluxes [Jy]	AARTFAAC flux density [Jy]
J0027+643	28.24 ± 0.19	362.42 ± 0.27
-	17.62 ± 0.19	-
-	13.51 ± 0.20	-
J0110+134	56.78 ± 0.10	122.93 ± 0.23
-	23.69 ± 0.10	-
J0224+430	12.77 ± 0.15	96.47 ± 0.10
-	10.16 ± 0.16	-
J0400+105	23.88 ± 0.26	132.39 ± 0.15
-	10.85 ± 0.26	-
J0420+381	38.76 ± 0.21	167.93 ± 0.09
-	29.24 ± 0.21	-
-	13.44 ± 0.21	-
J0506+381	86.76 ± 0.24	237.15 ± 0.13
-	25.40 ± 0.24	-
-	14.56 ± 0.24	-
-	11.31 ± 0.24	-
J0627+401	16.76 ± 0.10	44.95 ± 0.06
-	16.31 ± 0.09	-
J0657+542	39.71 ± 0.09	56.75 ± 0.06
-	12.61 ± 0.10	-
J0829+292	19.55 ± 0.10	39.14 ± 0.08
-	15.38 ± 0.10	-
J0855+139	40.21 ± 0.17	64.32 ± 0.13
-	15.17 ± 0.18	-
J1144+218	30.70 ± 0.14	50.02 ± 0.16
-	16.40 ± 0.13	-
J1445+768	18.67 ± 0.13	45.58 ± 0.10
-	14.72 ± 0.14	-
J1506+259	28.97 ± 0.12	127.36 ± 0.13
-	11.99 ± 0.12	-
J1552+050	373.91 ± 0.49	873.07 ± 0.37
-	309.02 ± 0.51	-
J1840+797	22.01 ± 0.32	117.25 ± 0.14
-	18.60 ± 0.31	-
-	10.92 ± 0.31	-
J2247+397	34.83 ± 0.18	150.89 ± 0.15
-	25.58 ± 0.19	-
-	25.46 ± 0.18	-

Table 5. A list of sources in the AARTFAAC catalogue which are known to be composed of two or more VLSSr sources, blended together. A threshold of 10 Jy was used to filter the VLSSr catalogue in order to limit the number of objects compared. This threshold is motivated by the fact that a source below 10 Jy at 74 MHz would, given the sensitivity of AARTFAAC, likely not have a strong contribution to the observed flux density.

ments to well studied flux calibrators. Here we collect and summarize our findings on these aspects:

Instrumental flux stability: We collected data from all LSTs, over a 3-month period, and find that longer-time average fluxes show no trends with time or Zenith angle at levels above 1%, so indeed our measurements and instrumental calibration are quite stable (Figs. 3 and 5). Furthermore, we see that for bright sources the error estimates on 1-second measurements are a bit larger than the measured flux variations on short time scales (Fig. 5), so our error estimates are somewhat conservative.

Ionospheric effects: We have used data from representative ionospheric weather, however excluding periods of either strong RFI or ionospheric turbulence around the A-team sources which resulted the data being flagged by the corre-

lator or calibration pipelines, and no images being created. We see that in these data, the dominant timescale for ionospheric variations is of order 15 minutes at our observing frequency (60 MHz) and the typical amplitude is 10–15%, somewhat larger than the instantaneous flux measurement accuracy of bright sources (Fig. 5). We also find that these variations are spatially uncorrelated on scales more than 5 degrees. This is why we employ the strategy of fitting instantaneous flux scales using all available AARTFAAC catalogue sources at any time: it decreases the uncertainty in the calibration scale factor and prevents the scintillation variations of a single calibrator to dominate the flux scale. Because we do this every second and monitor the variations, we are provided with an automatic assessment of ionospheric conditions, which is also used by LOFAR. These effects are much less in MWA at somewhat higher frequencies, see (Loi et al. 2015c), indicating that even within the LOFAR low band the strength will vary significantly with frequency.

Absolute calibration: To tie the AARTFAAC flux scale to more widely applicable radio flux calibrations, we compared our fluxes to a number of previously established radio catalogues. We had to fit models and interpolate, since very few previous measurements are available at 60 MHz (sect. 5). In table 3, we can see the precision and stability of our measurements is indeed very good compared to previous work, but that the calibrations of different very bright Northern sources differ by a few to 10% between papers, and in a few cases more (specifically our flux for 3C286 seems anomalously high compared to other work). Absolute flux calibration at these radio frequencies thus appears to be mostly reliable to 10%.

6 CONCLUSION

This work presents the method used for calibrating the flux density scale of AARTFAAC images in real-time, for the upcoming transient and variability surveys. Additionally, the AARTFAAC catalogue of calibration sources is presented.

Due to the lack of a sufficient number of well measured calibrator sources at low frequencies, and the requirement that AARTFAAC images are calibrated in real-time, a bootstrap algorithm was used. Hence, the AARTFAAC catalogue is fundamentally based on a flux density scaling derived from the spectral fits published by Perley & Butler (2017). Consequently, any systematic bias in the fluxes reported there could influence the AARTFAAC catalogue. Therefore, as a verification the AARTFAAC catalogue was compared to the larger, but less precise, catalogue of Helmboldt et al. (2008). Here good agreement was found between the spectral fit extrapolated to 60 MHz and the measurements presented in this work. However, a tendency for AARTFAAC to measure more flux was observed. This is potentially explained by the much higher density of the LOFAR superterp resulting in higher sensitivity to diffuse emission. Therefore, it is shown that AARTFAAC is capable of filling the gap between 38 and 74 MHz and providing an accurate flux density scale for the calibration of densely packed low-frequency arrays.

Additionally, statistical analysis of the times series of flux density measurements for each source resulted in insights into the effect of ionospheric variability. Significantly, it was observed that such variability preferentially skews the

distribution of measurements in the positive direction, giving the average a positive bias. Consequently, it was found that the most robust method to mitigate this was to fit a skew normal distribution, and calculate the mode. In light of this, observations which attempt to achieve high sensitivity with long integrations, without correcting for ionospheric variability on short timescales, will also have a positive bias.

For our ability to detect new transients, the flux calibration is of minor importance, because this depends only on the ability to detect a new source against the local noise. The main limitations for this are (i) that we examine large volumes of data, so we typically have to set the threshold at 8 times the local RMS to avoid many false positives, and (ii) that we have to distinguish transients from RFI, terrestrial sources and artifacts. But if we do detect a source, the instantaneous flux uncertainty on second time scales will be dominated by the ionosphere for bright sources, and roughly equally by the ionospheric and measurement noise near the threshold. The ionospheric uncertainty decreases significantly only when the sources stay on for longer than the typical variation time of 15 minutes.

In the future this work may be extended by incorporating more data. Given that the primary science goal of AARTFAAC is to survey the sky for transient and variable sources, many hundreds of hours of observations will be made. This enormous amount of data will allow for extremely precise flux density values to be measured.

Lastly, observations across the entire frequency range of the LOFAR LBA 10-90 MHz would allow highly accurate spectra to be fit, however at the low end of the bandpass Perley & Butler (2017) would no longer be a suitable reference catalogue. Lastly, the planned upgrade of AARTFAAC to include 12 stations of the LOFAR core, rather than the six currently in operation, will produce images of higher sensitivity and resolution. This will allow for the measurement of currently blended sources, and many which are now below our detection threshold.

ACKNOWLEDGEMENTS

This work is funded by the ERC Advanced Investigator grant no. 247295 awarded to Prof. Ralph Wijers, University of Amsterdam. We thank The Netherlands Institute for Radio Astronomy (ASTRON) for support provided in carrying out the commissioning observations.

The authors would also like to thank the LOFAR science support for their assistance in obtaining and processing the data used in this work. We use data obtained from LOFAR, the Low Frequency Array designed and constructed by ASTRON, which has facilities in several countries, that are owned by various parties (each with their own funding sources), and that are collectively operated by the International LOFAR Telescope (ILT) foundation under a joint scientific policy.

REFERENCES

- Bell M. E., et al., 2014, *MNRAS*, **438**, 352
 Carbone D., et al., 2016, *MNRAS*, **459**, 3161
 Carbone D., et al., 2018, *Astronomy and Computing*, **23**, 92
 Eastwood M. W., et al., 2018, *AJ*, **156**, 32

- Green D. A., 2014, *Bulletin of the Astronomical Society of India*, **42**, 47
 Helmboldt J. F., Kassim N. E., Cohen A. S., Lane W. M., Lazio T. J., 2008, *ApJS*, **174**, 313
 Hyman S. D., Lazio T. J. W., Kassim N. E., Ray P. S., Markwardt C. B., Yusef-Zadeh F., 2005, *Nature*, **434**, 50
 Klein U., Emerson D. T., Haslam C. G. T., Salter C. J., 1979, *A&A*, **76**, 120
 Lane W. M., Cotton W. D., van Velzen S., Clarke T. E., Kassim N. E., Helmboldt J. F., Lazio T. J. W., Cohen A. S., 2014, *MNRAS*, **440**, 327
 Loi S. T., et al., 2015a, *Geophysical Research Letters*, **42**, 3707
 Loi S. T., et al., 2015b, *Radio Science*, **50**, 574
 Loi S. T., et al., 2015c, *MNRAS*, **453**, 2731
 Murphy T., et al., 2017, *MNRAS*, **466**, 1944
 Obenberger K. S., et al., 2014, *ApJ*, **788**, L26
 Obenberger K. S., et al., 2015, *Journal of Astronomical Instrumentation*, **4**, 1550004
 Offringa A. R., et al., 2013, *A&A*, **549**, A11
 Ott M., Witzel A., Quirrenbach A., Krichbaum T. P., Standke K. J., Schalinski C. J., Hummel C. A., 1994, *A&A*, **284**, 331
 Patil A. H., et al., 2017, *ApJ*, **838**, 65
 Perley R. A., Butler B. J., 2017, *ApJS*, **230**, 7
 Petroff E., et al., 2015, *MNRAS*, **447**, 246
 Pietka et al. 2015, *MNRAS*, **446**, 3687
 Prasad P., Wijnholds S. J., Huizinga F., Wijers R. A. M. J., 2014, *A&A*, **568**, A48
 Prasad P., et al., 2016, *Journal of Astronomical Instrumentation*, **5**, 1641008
 Rees N., 1990, *MNRAS*, **244**, 233
 Rowlinson A., et al., 2016, *MNRAS*, **458**, 3506
 Salvatier J., Wiecki T., Fonnesbeck C., 2015, preprint, ([arXiv:1507.08050](https://arxiv.org/abs/1507.08050))
 Scaife A. M. M., Heald G. H., 2012, *MNRAS*, **423**, L30
 Stewart et al. 2016, *MNRAS*, **456**, 2321
 Swinbank J. D., et al., 2015, *Astronomy and Computing*, **11**, 25
 van Haarlem M. P., et al., 2013, *A&A*, **556**, A2

APPENDIX A: SUPPLEMENTARY ONLINE MATERIAL: AARTFAAC CATALOGUE

Label	Ra [$^{\circ}$]	Dec [$^{\circ}$]	Flux density [Jy]	Location ξ	Scale ω	Shape α	Name	Measurements #
J0007+725	1.96 \pm 0.36	72.53 \pm 0.12	86.17 \pm 0.13	75.94 \pm 0.09	22.17 \pm 0.09	3.27 \pm 0.05	CTA 1	72070
J0027+642	6.78 \pm 0.10	64.22 \pm 0.10	362.42 \pm 0.27	336.64 \pm 0.31	48.75 \pm 0.27	2.10 \pm 0.04	Tycho SNR	55465
J0044+521	11.19 \pm 0.05	52.20 \pm 0.11	70.75 \pm 0.09	63.80 \pm 0.08	14.30 \pm 0.08	2.86 \pm 0.05	3C20	35940
J0057+266	14.45 \pm 0.06	26.66 \pm 0.09	72.75 \pm 0.14	65.78 \pm 0.30	13.20 \pm 0.20	1.17 \pm 0.06	3C28	18137
J0058+683	14.64 \pm 0.20	68.39 \pm 0.11	91.20 \pm 0.08	85.74 \pm 0.26	11.45 \pm 0.14	0.86 \pm 0.05	3C27	41301
J0110+322	17.54 \pm 0.09	32.26 \pm 0.11	61.68 \pm 0.12	55.01 \pm 0.12	12.99 \pm 0.11	2.39 \pm 0.07	3C34	19807
J0110+134	17.59 \pm 0.03	13.45 \pm 0.09	122.93 \pm 0.23	111.74 \pm 0.34	20.57 \pm 0.27	1.58 \pm 0.06	3C33	11207
J0127+332	21.97 \pm 0.12	33.30 \pm 0.13	51.72 \pm 0.14	47.55 \pm 0.22	7.68 \pm 0.17	1.54 \pm 0.11	3C41	5048
J0137+210	24.47 \pm 0.04	21.08 \pm 0.07	89.87 \pm 0.18	79.84 \pm 0.23	18.60 \pm 0.19	1.83 \pm 0.06	3C47	16127
J0139+332	24.84 \pm 0.04	33.29 \pm 0.10	81.36 \pm 0.33	62.62 \pm 0.26	39.52 \pm 0.26	3.05 \pm 0.07	3C48	25907
J0158+289	29.65 \pm 0.05	28.96 \pm 0.09	48.71 \pm 0.14	42.46 \pm 0.14	12.04 \pm 0.13	2.28 \pm 0.08	3C55	14031
J0220+625	35.09 \pm 0.09	62.54 \pm 0.12	158.57 \pm 0.18	142.35 \pm 0.16	33.87 \pm 0.16	2.97 \pm 0.05	HB3	48715
J0224+430	36.13 \pm 0.05	43.06 \pm 0.10	96.47 \pm 0.10	88.40 \pm 0.09	17.03 \pm 0.09	3.06 \pm 0.05	3C66	36406
J0224+401	36.19 \pm 0.07	40.15 \pm 0.07	55.38 \pm 0.08	49.47 \pm 0.06	13.53 \pm 0.08	3.72 \pm 0.07	3C65	27047
J0225+863	36.30 \pm 1.41	86.36 \pm 0.09	100.86 \pm 0.09	108.41 \pm 0.37	16.51 \pm 0.18	-0.78 \pm 0.04	-	121716
J0234+346	38.51 \pm 0.06	34.60 \pm 0.09	45.81 \pm 0.10	41.18 \pm 0.09	9.28 \pm 0.09	2.63 \pm 0.08	-	14837
J0235+317	38.96 \pm 0.06	31.71 \pm 0.06	45.11 \pm 0.14	40.65 \pm 0.22	8.22 \pm 0.16	1.48 \pm 0.10	-	7556
J0240+593	40.10 \pm 0.08	59.37 \pm 0.06	56.82 \pm 0.08	52.41 \pm 0.09	8.43 \pm 0.08	2.19 \pm 0.06	3C69	18542
J0258+062	44.71 \pm 0.03	6.23 \pm 0.06	80.23 \pm 0.21	74.50 \pm 0.59	11.38 \pm 0.34	1.00 \pm 0.12	3C75	7650
J0302+508	45.65 \pm 0.09	50.87 \pm 0.07	50.00 \pm 0.09	45.79 \pm 0.15	7.78 \pm 0.11	1.41 \pm 0.07	3C76	10737
J0311+171	47.85 \pm 0.03	17.19 \pm 0.06	68.23 \pm 0.10	62.32 \pm 0.16	10.87 \pm 0.12	1.49 \pm 0.05	3C79	20126
J0321+416	50.29 \pm 0.02	41.69 \pm 0.08	306.40 \pm 0.12	295.88 \pm 0.19	19.35 \pm 0.15	1.49 \pm 0.04	3C84	34840
J0329+553	52.43 \pm 0.06	55.38 \pm 0.08	84.62 \pm 0.07	78.45 \pm 0.11	11.36 \pm 0.09	1.44 \pm 0.03	3C86	41894
J0349+680	57.27 \pm 0.17	68.10 \pm 0.08	48.34 \pm 0.06	47.26 \pm 1.02	5.11 \pm 0.19	0.30 \pm 0.28	-	16358
J0400+105	60.09 \pm 0.02	10.53 \pm 0.05	132.39 \pm 0.15	125.67 \pm 0.31	12.73 \pm 0.20	1.18 \pm 0.07	3C98	18238
J0409+430	62.46 \pm 0.04	43.09 \pm 0.08	76.12 \pm 0.09	69.52 \pm 0.13	12.13 \pm 0.10	1.53 \pm 0.04	3C103	36700
J0415+112	63.77 \pm 0.03	11.21 \pm 0.07	69.68 \pm 0.06	70.33 \pm 1.43	6.60 \pm 0.19	-0.14 \pm 0.29	3C109	16943
J0420+381	65.04 \pm 0.02	38.14 \pm 0.08	167.93 \pm 0.09	161.74 \pm 0.30	12.90 \pm 0.16	0.87 \pm 0.05	3C111	35165
J0428+769	67.22 \pm 0.72	76.94 \pm 0.16	46.53 \pm 0.12	41.60 \pm 0.07	14.78 \pm 0.09	6.08 \pm 0.16	-	19722
J0438+297	69.67 \pm 0.02	29.75 \pm 0.07	462.85 \pm 0.33	438.11 \pm 0.49	45.47 \pm 0.37	1.59 \pm 0.04	3C123	33194
J0438+726	69.68 \pm 0.22	72.62 \pm 0.08	45.49 \pm 0.09	41.83 \pm 0.13	6.74 \pm 0.10	1.64 \pm 0.08	-	10510
J0450+450	72.66 \pm 0.03	45.08 \pm 0.07	106.13 \pm 0.08	100.43 \pm 0.19	11.00 \pm 0.12	1.08 \pm 0.04	3C129	39028
J0455+521	73.80 \pm 0.06	52.14 \pm 0.07	57.49 \pm 0.06	52.70 \pm 0.07	8.96 \pm 0.06	1.94 \pm 0.04	3C130	35922
J0456+579	74.09 \pm 0.10	58.00 \pm 0.06	43.06 \pm 0.09	40.35 \pm 0.12	5.01 \pm 0.09	1.75 \pm 0.10	-	6789
J0503+465	75.81 \pm 0.06	46.56 \pm 0.09	143.52 \pm 0.10	133.65 \pm 0.11	19.15 \pm 0.10	2.35 \pm 0.04	HB9	40246
J0504+252	76.12 \pm 0.04	25.28 \pm 0.08	56.06 \pm 0.17	50.56 \pm 0.18	10.56 \pm 0.17	2.25 \pm 0.11	3C133	6752
J0506+381	76.61 \pm 0.02	38.16 \pm 0.07	237.15 \pm 0.13	226.26 \pm 0.20	20.02 \pm 0.16	1.50 \pm 0.04	3C134	37471
J0507+631	76.90 \pm 0.09	63.13 \pm 0.08	39.66 \pm 0.09	36.57 \pm 0.09	6.08 \pm 0.08	2.47 \pm 0.10	-	7826
J0518+249	79.52 \pm 0.04	24.98 \pm 0.06	59.88 \pm 0.09	55.79 \pm 0.15	7.57 \pm 0.10	1.38 \pm 0.06	-	12926
J0527+329	81.79 \pm 0.19	32.94 \pm 0.10	56.77 \pm 0.12	52.14 \pm 0.15	8.61 \pm 0.12	1.90 \pm 0.09	3C141	10846
J0532+065	83.23 \pm 0.04	6.56 \pm 0.06	60.90 \pm 0.16	54.45 \pm 0.24	11.86 \pm 0.17	1.58 \pm 0.08	-	15398

continued ...

... continued

Label	Ra [$^{\circ}$]	Dec [$^{\circ}$]	Flux density [Jy]	Location ξ	Scale ω	Shape α	Name	Measurements #
J0544+498	86.08 \pm 0.06	49.82 \pm 0.07	48.71 \pm 0.14	41.63 \pm 0.10	15.96 \pm 0.10	3.59 \pm 0.10	3C147	26781
J0611+480	92.85 \pm 0.08	48.05 \pm 0.07	46.02 \pm 0.05	42.15 \pm 0.10	7.17 \pm 0.07	1.33 \pm 0.04	3C153	31415
J0618+225	94.70 \pm 0.02	22.59 \pm 0.07	467.75 \pm 0.16	454.06 \pm 0.25	25.17 \pm 0.20	1.52 \pm 0.04	IC443, 3C157	33454
J0627+401	96.76 \pm 0.05	40.20 \pm 0.06	44.95 \pm 0.06	40.34 \pm 0.08	8.63 \pm 0.06	1.99 \pm 0.05	3C159	32863
J0646+213	101.69 \pm 0.05	21.35 \pm 0.08	61.08 \pm 0.12	55.26 \pm 0.17	10.70 \pm 0.13	1.61 \pm 0.06	3C166	15903
J0657+693	104.27 \pm 0.22	69.31 \pm 0.07	37.17 \pm 0.08	34.50 \pm 0.12	4.91 \pm 0.09	1.65 \pm 0.10	3C169	8040
J0657+542	104.47 \pm 0.09	54.23 \pm 0.09	56.75 \pm 0.06	51.24 \pm 0.11	10.21 \pm 0.08	1.34 \pm 0.03	3C171	55924
J0703+251	105.89 \pm 0.05	25.19 \pm 0.07	48.29 \pm 0.08	43.40 \pm 0.10	9.04 \pm 0.08	1.79 \pm 0.05	3C172	26701
J0707+633	106.85 \pm 0.12	63.32 \pm 0.07	39.24 \pm 0.05	35.81 \pm 0.09	6.31 \pm 0.07	1.46 \pm 0.05	-	26647
J0709+425	107.26 \pm 0.08	42.53 \pm 0.09	43.76 \pm 0.06	40.37 \pm 0.11	6.33 \pm 0.07	1.27 \pm 0.05	-	27363
J0712+748	108.06 \pm 0.29	74.83 \pm 0.10	53.18 \pm 0.06	47.56 \pm 0.10	10.33 \pm 0.07	1.47 \pm 0.03	-	74465
J0714+116	108.62 \pm 0.04	11.67 \pm 0.08	73.94 \pm 0.13	67.27 \pm 0.28	12.52 \pm 0.18	1.23 \pm 0.06	3C175	22802
J0731+246	112.75 \pm 0.05	24.61 \pm 0.07	41.16 \pm 0.08	37.80 \pm 0.12	6.18 \pm 0.09	1.50 \pm 0.07	-	15365
J0742+702	115.69 \pm 0.15	70.30 \pm 0.07	39.44 \pm 0.08	34.67 \pm 0.07	9.52 \pm 0.07	2.60 \pm 0.06	3C184	35689
J0746+377	116.54 \pm 0.05	37.79 \pm 0.08	49.35 \pm 0.09	42.72 \pm 0.08	13.42 \pm 0.08	2.72 \pm 0.05	3C186	39665
J0747+804	116.91 \pm 0.35	80.40 \pm 0.08	46.89 \pm 0.06	42.43 \pm 0.08	8.27 \pm 0.06	1.83 \pm 0.05	-	43127
J0750+558	117.74 \pm 0.07	55.84 \pm 0.07	54.34 \pm 0.05	50.14 \pm 0.13	8.13 \pm 0.08	1.06 \pm 0.04	-	57674
J0800+377	120.10 \pm 0.06	37.70 \pm 0.10	41.59 \pm 0.08	37.57 \pm 0.08	7.80 \pm 0.08	2.36 \pm 0.07	3C189	14698
J0802+141	120.73 \pm 0.04	14.13 \pm 0.08	50.68 \pm 0.12	44.82 \pm 0.10	12.46 \pm 0.10	3.13 \pm 0.09	3C190	16759
J0802+614	120.74 \pm 0.17	61.48 \pm 0.08	42.35 \pm 0.10	38.93 \pm 0.14	6.29 \pm 0.11	1.65 \pm 0.09	-	7457
J0806+103	121.53 \pm 0.05	10.31 \pm 0.07	57.86 \pm 0.15	50.79 \pm 0.15	13.76 \pm 0.14	2.37 \pm 0.08	3C191	16142
J0807+241	121.79 \pm 0.04	24.14 \pm 0.09	65.78 \pm 0.06	66.86 \pm 1.78	9.36 \pm 0.22	-0.16 \pm 0.25	3C192	41548
J0811+423	122.91 \pm 0.08	42.35 \pm 0.07	46.74 \pm 0.07	49.85 \pm 0.23	6.30 \pm 0.13	-0.94 \pm 0.08	-	14116
J0815+481	123.85 \pm 0.04	48.19 \pm 0.08	157.30 \pm 0.20	140.87 \pm 0.31	30.19 \pm 0.23	1.61 \pm 0.04	3C196	60025
J0823+056	125.96 \pm 0.05	5.70 \pm 0.11	65.44 \pm 0.16	59.29 \pm 0.17	11.86 \pm 0.15	2.28 \pm 0.09	3C198	10087
J0829+292	127.30 \pm 0.05	29.27 \pm 0.07	39.14 \pm 0.08	35.66 \pm 0.10	6.52 \pm 0.08	1.98 \pm 0.08	3C200	11094
J0839+651	129.99 \pm 0.14	65.17 \pm 0.08	41.06 \pm 0.04	37.68 \pm 0.08	6.32 \pm 0.05	1.25 \pm 0.04	3C204	41604
J0841+578	130.39 \pm 0.10	57.89 \pm 0.11	43.48 \pm 0.07	37.62 \pm 0.10	10.77 \pm 0.08	1.64 \pm 0.04	3C205	49824
J0852+784	133.11 \pm 0.41	78.44 \pm 0.10	47.80 \pm 0.06	43.96 \pm 0.10	7.08 \pm 0.07	1.46 \pm 0.05	-	29914
J0855+139	133.77 \pm 0.05	13.90 \pm 0.08	64.32 \pm 0.13	56.72 \pm 0.17	14.08 \pm 0.14	1.82 \pm 0.06	3C208	22018
J0859+277	134.97 \pm 0.05	27.80 \pm 0.07	36.80 \pm 0.14	33.13 \pm 0.14	7.18 \pm 0.13	2.40 \pm 0.15	3C210	4901
J0910+428	137.74 \pm 0.09	42.82 \pm 0.11	62.86 \pm 0.14	52.63 \pm 0.12	20.55 \pm 0.11	2.65 \pm 0.05	3C216	52948
J0912+377	138.09 \pm 0.08	37.79 \pm 0.09	63.12 \pm 0.12	54.60 \pm 0.08	21.17 \pm 0.09	4.39 \pm 0.08	3C217	55956
J0918+585	139.52 \pm 0.14	58.55 \pm 0.07	36.62 \pm 0.11	35.07 \pm 1.28	5.57 \pm 0.30	0.43 \pm 0.34	-	6146
J0922+456	140.74 \pm 0.05	45.60 \pm 0.10	114.71 \pm 0.12	121.98 \pm 0.87	19.24 \pm 0.34	-0.57 \pm 0.07	3C219	62283
J0936+790	144.24 \pm 0.39	79.03 \pm 0.10	57.90 \pm 0.05	52.45 \pm 0.07	10.01 \pm 0.05	1.57 \pm 0.03	-	76940
J0941+358	145.38 \pm 0.06	35.84 \pm 0.08	40.38 \pm 0.09	35.13 \pm 0.05	14.58 \pm 0.07	5.38 \pm 0.10	-	41495
J0943+137	145.95 \pm 0.05	13.79 \pm 0.09	55.56 \pm 0.15	47.24 \pm 0.13	16.77 \pm 0.12	2.68 \pm 0.07	3C225	23350
J0943+831	145.97 \pm 0.59	83.18 \pm 0.10	59.12 \pm 0.05	53.30 \pm 0.09	10.70 \pm 0.06	1.47 \pm 0.03	-	88487
J0945+097	146.35 \pm 0.05	9.71 \pm 0.06	57.78 \pm 0.17	50.83 \pm 0.15	14.01 \pm 0.14	2.68 \pm 0.09	3C226	13561
J0949+073	147.37 \pm 0.04	7.36 \pm 0.07	113.72 \pm 0.12	106.25 \pm 0.17	13.73 \pm 0.14	1.65 \pm 0.05	3C227	18700
J0951+143	147.95 \pm 0.06	14.34 \pm 0.09	50.78 \pm 0.10	45.14 \pm 0.11	10.71 \pm 0.09	2.14 \pm 0.06	3C228	22500

continued ...

... continued

Label	Ra [$^{\circ}$]	Dec [$^{\circ}$]	Flux density [Jy]	Location ξ	Scale ω	Shape α	Name	Measurements #
J0952+731	148.11 \pm 0.21	73.18 \pm 0.10	49.90 \pm 0.04	47.81 \pm 0.41	6.19 \pm 0.13	0.49 \pm 0.10	-	64167
J0958+694	149.70 \pm 0.17	69.48 \pm 0.09	41.65 \pm 0.07	37.83 \pm 0.15	7.14 \pm 0.10	1.27 \pm 0.06	3C231	24283
J1003+287	150.85 \pm 0.05	28.72 \pm 0.08	90.06 \pm 0.15	76.73 \pm 0.11	31.20 \pm 0.14	3.90 \pm 0.06	3C234	47323
J1006+225	151.53 \pm 0.23	22.54 \pm 0.09	46.39 \pm 0.20	40.41 \pm 0.28	11.03 \pm 0.21	1.71 \pm 0.11	-	13088
J1007+347	151.94 \pm 0.08	34.78 \pm 0.09	39.54 \pm 0.11	34.27 \pm 0.06	16.44 \pm 0.08	6.49 \pm 0.14	-	29749
J1011+068	152.77 \pm 0.24	6.88 \pm 0.38	61.42 \pm 0.22	52.52 \pm 0.23	17.18 \pm 0.21	2.31 \pm 0.09	3C237	10461
J1013+463	153.39 \pm 0.09	46.34 \pm 0.09	46.28 \pm 0.08	39.62 \pm 0.07	13.44 \pm 0.07	2.70 \pm 0.05	-	49609
J1016+745	154.15 \pm 0.30	74.56 \pm 0.11	42.11 \pm 0.14	37.26 \pm 0.13	9.64 \pm 0.12	2.56 \pm 0.12	-	15676
J1020+808	155.09 \pm 0.65	80.83 \pm 0.14	52.86 \pm 0.11	46.47 \pm 0.08	14.22 \pm 0.09	3.48 \pm 0.08	-	28682
J1027+064	156.89 \pm 0.04	6.49 \pm 0.09	54.13 \pm 0.13	49.08 \pm 0.17	9.39 \pm 0.14	1.88 \pm 0.09	3C243	8357
J1035+581	158.84 \pm 0.10	58.19 \pm 0.10	58.04 \pm 0.09	50.83 \pm 0.24	13.91 \pm 0.14	1.08 \pm 0.04	-	73615
J1044+118	161.09 \pm 0.05	11.86 \pm 0.10	42.83 \pm 0.14	38.72 \pm 0.12	8.52 \pm 0.12	2.91 \pm 0.14	3C245	5979
J1108+768	167.23 \pm 0.31	76.86 \pm 0.10	51.76 \pm 0.05	46.84 \pm 0.09	9.14 \pm 0.06	1.31 \pm 0.03	-	62816
J1110+249	167.61 \pm 0.07	24.96 \pm 0.08	48.67 \pm 0.08	42.94 \pm 0.08	11.28 \pm 0.07	2.50 \pm 0.05	3C250	34110
J1113+355	168.29 \pm 0.07	35.59 \pm 0.09	41.12 \pm 0.12	35.15 \pm 0.06	21.53 \pm 0.09	8.05 \pm 0.16	3C252	41489
J1115+405	168.93 \pm 0.07	40.58 \pm 0.09	61.78 \pm 0.15	50.50 \pm 0.09	31.24 \pm 0.12	5.34 \pm 0.08	3C254	61784
J1141+657	175.32 \pm 0.18	65.71 \pm 0.09	50.40 \pm 0.07	43.84 \pm 0.12	12.07 \pm 0.08	1.46 \pm 0.03	3C263	73340
J1144+218	176.09 \pm 0.07	21.89 \pm 0.09	50.02 \pm 0.16	42.33 \pm 0.10	20.27 \pm 0.13	4.91 \pm 0.12	-	20454
J1146+195	176.60 \pm 0.05	19.59 \pm 0.09	80.30 \pm 0.13	69.63 \pm 0.15	20.26 \pm 0.13	2.13 \pm 0.04	3C264	39290
J1146+315	176.75 \pm 0.05	31.54 \pm 0.09	60.55 \pm 0.11	52.09 \pm 0.16	15.60 \pm 0.12	1.70 \pm 0.05	3C265	49055
J1147+496	176.84 \pm 0.07	49.65 \pm 0.06	36.86 \pm 0.15	31.98 \pm 0.12	10.44 \pm 0.12	3.18 \pm 0.13	-	8194
J1151+127	177.84 \pm 0.05	12.74 \pm 0.09	49.69 \pm 0.15	44.88 \pm 0.19	8.89 \pm 0.16	1.80 \pm 0.10	3C267	5008
J1156+547	179.17 \pm 0.10	54.76 \pm 0.08	36.21 \pm 0.08	31.97 \pm 0.06	9.59 \pm 0.07	3.61 \pm 0.09	-	19741
J1200+729	180.25 \pm 0.24	72.93 \pm 0.11	54.85 \pm 0.09	47.09 \pm 0.14	14.26 \pm 0.10	1.59 \pm 0.04	-	91796
J1210+436	182.68 \pm 0.07	43.62 \pm 0.06	33.98 \pm 0.10	30.00 \pm 0.09	8.13 \pm 0.08	2.80 \pm 0.10	-	11854
J1217+534	184.36 \pm 0.09	53.46 \pm 0.05	34.14 \pm 0.12	31.09 \pm 0.13	5.90 \pm 0.12	2.31 \pm 0.15	-	4537
J1220+057	185.17 \pm 0.06	5.77 \pm 0.09	123.19 \pm 0.14	113.56 \pm 0.18	17.76 \pm 0.15	1.72 \pm 0.05	3C270	20649
J1222+336	185.51 \pm 0.05	33.62 \pm 0.06	37.49 \pm 0.11	32.39 \pm 0.09	11.15 \pm 0.09	3.35 \pm 0.10	-	15260
J1236+212	189.21 \pm 0.06	21.23 \pm 0.08	46.24 \pm 0.10	40.99 \pm 0.11	9.93 \pm 0.09	2.10 \pm 0.06	-	18931
J1245+163	191.30 \pm 0.06	16.33 \pm 0.09	54.99 \pm 0.23	48.99 \pm 0.34	11.05 \pm 0.25	1.60 \pm 0.12	-	4432
J1255+156	193.76 \pm 0.07	15.64 \pm 0.08	51.29 \pm 0.18	46.39 \pm 0.24	9.05 \pm 0.19	1.75 \pm 0.12	-	44450
J1257+473	194.42 \pm 0.09	47.31 \pm 0.10	55.22 \pm 0.11	45.59 \pm 0.08	21.78 \pm 0.08	3.61 \pm 0.05	3C280	67093
J1259+278	194.97 \pm 0.13	27.82 \pm 0.08	58.63 \pm 0.06	59.12 \pm 1.54	10.83 \pm 0.12	-0.06 \pm 0.18	-	34053
J1312+273	198.04 \pm 0.07	27.40 \pm 0.07	43.60 \pm 0.11	38.86 \pm 0.12	8.96 \pm 0.11	2.09 \pm 0.08	3C284	11552
J1332+305	203.01 \pm 0.09	30.52 \pm 0.09	47.69 \pm 0.12	41.59 \pm 0.10	12.27 \pm 0.10	2.67 \pm 0.07	3C286	21608
J1336+409	204.08 \pm 0.10	40.93 \pm 0.06	34.73 \pm 0.11	31.98 \pm 0.15	5.09 \pm 0.12	1.75 \pm 0.13	-	3943
J1340+387	205.07 \pm 0.07	38.79 \pm 0.08	48.08 \pm 0.07	46.33 \pm 1.39	8.54 \pm 0.25	0.28 \pm 0.22	3C288	31456
J1346+496	206.71 \pm 0.09	49.65 \pm 0.06	40.64 \pm 0.13	37.04 \pm 0.23	6.69 \pm 0.16	1.35 \pm 0.11	-	5813
J1351+643	207.78 \pm 0.15	64.36 \pm 0.09	47.26 \pm 0.07	42.09 \pm 0.15	9.85 \pm 0.10	1.14 \pm 0.04	3C292	45160
J1354+315	208.66 \pm 0.13	31.54 \pm 0.08	50.76 \pm 0.09	47.04 \pm 0.36	8.03 \pm 0.18	0.81 \pm 0.09	3C293	16714
J1407+341	211.89 \pm 0.08	34.13 \pm 0.07	48.77 \pm 0.14	41.17 \pm 0.15	14.38 \pm 0.12	2.11 \pm 0.06	3C294	31019
J1410+313	212.67 \pm 0.08	31.33 \pm 0.08	46.28 \pm 0.22	48.81 \pm 1.62	7.01 \pm 0.50	-0.62 \pm 0.38	-	4231

continued ...

... continued

Label	Ra [$^{\circ}$]	Dec [$^{\circ}$]	Flux density [Jy]	Location ξ	Scale ω	Shape α	Name	Measurements #
J1412+521	213.15 \pm 0.05	52.17 \pm 0.08	112.55 \pm 0.18	95.06 \pm 0.12	41.24 \pm 0.14	3.96 \pm 0.05	3C295	77864
J1420+064	215.11 \pm 0.04	6.48 \pm 0.07	86.31 \pm 0.39	67.76 \pm 0.27	43.04 \pm 0.29	3.82 \pm 0.10	3C298	21751
J1422+416	215.61 \pm 0.08	41.69 \pm 0.07	41.98 \pm 0.12	36.64 \pm 0.10	11.29 \pm 0.10	3.08 \pm 0.09	3C299	12810
J1424+195	216.18 \pm 0.06	19.52 \pm 0.11	60.66 \pm 0.18	51.91 \pm 0.09	27.69 \pm 0.12	6.63 \pm 0.14	-	35518
J1427+376	216.83 \pm 0.07	37.65 \pm 0.06	38.91 \pm 0.16	35.79 \pm 0.67	6.48 \pm 0.29	0.91 \pm 0.20	-	4503
J1444+519	221.04 \pm 0.09	51.98 \pm 0.07	39.45 \pm 0.16	35.18 \pm 0.13	8.99 \pm 0.14	3.03 \pm 0.15	3C303	5025
J1445+768	221.46 \pm 0.43	76.90 \pm 0.09	45.58 \pm 0.10	39.13 \pm 0.11	12.32 \pm 0.09	2.19 \pm 0.06	-	37122
J1449+631	222.47 \pm 0.20	63.18 \pm 0.08	43.26 \pm 0.08	37.74 \pm 0.06	12.35 \pm 0.06	3.53 \pm 0.06	3C305	33402
J1501+714	225.29 \pm 0.24	71.48 \pm 0.20	44.77 \pm 0.13	38.12 \pm 0.07	21.64 \pm 0.10	6.92 \pm 0.14	-	32787
J1506+259	226.55 \pm 0.03	25.97 \pm 0.07	127.36 \pm 0.13	112.69 \pm 0.11	31.71 \pm 0.12	3.25 \pm 0.04	3C310	57615
J1518+070	229.53 \pm 0.03	7.01 \pm 0.06	114.72 \pm 0.12	117.79 \pm 2.38	13.00 \pm 0.41	-0.33 \pm 0.25	3C317	31047
J1523+076	230.82 \pm 0.04	7.66 \pm 0.08	71.86 \pm 0.13	66.71 \pm 0.23	9.52 \pm 0.16	1.37 \pm 0.08	-	8780
J1525+543	231.31 \pm 0.09	54.38 \pm 0.08	46.64 \pm 0.04	47.26 \pm 1.18	7.23 \pm 0.13	-0.11 \pm 0.21	3C319	42515
J1533+239	233.26 \pm 0.06	23.96 \pm 0.08	57.89 \pm 0.13	49.36 \pm 0.10	19.71 \pm 0.10	3.79 \pm 0.07	3C321	40369
J1551+626	237.76 \pm 0.12	62.65 \pm 0.07	42.27 \pm 0.13	37.38 \pm 0.10	10.77 \pm 0.10	3.39 \pm 0.12	3C325	12332
J1611+658	242.77 \pm 0.14	65.88 \pm 0.10	50.32 \pm 0.10	42.51 \pm 0.05	24.82 \pm 0.08	6.67 \pm 0.09	3C330	69223
J1629+395	247.44 \pm 0.04	39.51 \pm 0.07	120.52 \pm 0.11	106.56 \pm 0.09	29.71 \pm 0.11	3.13 \pm 0.03	3C338	62467
J1629+823	247.49 \pm 0.56	82.32 \pm 0.06	46.36 \pm 0.08	43.33 \pm 0.12	5.57 \pm 0.09	1.55 \pm 0.08	-	8240
J1630+442	247.62 \pm 0.09	44.30 \pm 0.10	48.80 \pm 0.19	42.93 \pm 0.18	11.72 \pm 0.16	2.61 \pm 0.12	3C337	8597
J1652+050	253.12 \pm 0.02	5.01 \pm 0.05	873.07 \pm 0.37	863.96 \pm 7.50	39.98 \pm 1.35	0.32 \pm 0.26	3C348	23233
J1711+460	257.94 \pm 0.11	46.01 \pm 0.08	44.38 \pm 0.13	40.47 \pm 0.10	8.84 \pm 0.11	3.60 \pm 0.15	3C352	7215
J1725+508	261.27 \pm 0.14	50.84 \pm 0.07	41.84 \pm 0.20	36.15 \pm 0.12	14.58 \pm 0.14	4.66 \pm 0.19	3C356	7369
J1746+802	266.60 \pm 0.58	80.27 \pm 0.09	60.42 \pm 0.16	54.18 \pm 0.31	11.60 \pm 0.21	1.32 \pm 0.08	-	14183
J1830+487	277.65 \pm 0.04	48.74 \pm 0.08	136.75 \pm 0.09	127.96 \pm 0.19	16.70 \pm 0.12	1.15 \pm 0.03	3C380	62202
J1836+326	279.13 \pm 0.07	32.69 \pm 0.08	56.65 \pm 0.22	50.16 \pm 0.15	15.77 \pm 0.17	4.20 \pm 0.17	-	7804
J1840+797	280.22 \pm 0.55	79.78 \pm 0.07	117.25 \pm 0.14	104.40 \pm 0.14	24.73 \pm 0.12	2.27 \pm 0.04	-	121769
J1844+455	281.22 \pm 0.07	45.56 \pm 0.06	54.96 \pm 0.07	49.80 \pm 0.07	10.00 \pm 0.07	2.35 \pm 0.05	3C388	24996
J1941+607	295.42 \pm 0.14	60.71 \pm 0.09	44.88 \pm 0.08	40.55 \pm 0.11	7.97 \pm 0.09	1.70 \pm 0.06	3C401	17535
J1955+328	298.93 \pm 0.08	32.88 \pm 0.10	114.73 \pm 0.24	115.93 \pm 3.51	12.29 \pm 0.54	-0.15 \pm 0.40	CTB 80	5553
J2015+236	303.94 \pm 0.03	23.61 \pm 0.07	206.18 \pm 0.20	214.69 \pm 2.21	21.56 \pm 0.54	-0.62 \pm 0.15	3C409	30016
J2020+455	305.17 \pm 0.04	45.56 \pm 0.08	288.53 \pm 0.13	277.60 \pm 0.30	21.02 \pm 0.19	1.09 \pm 0.04	W63	50894
J2021+297	305.39 \pm 0.05	29.73 \pm 0.06	103.62 \pm 0.14	97.94 \pm 0.43	11.31 \pm 0.25	0.98 \pm 0.09	3C410	17491
J2022+403	305.61 \pm 0.02	40.37 \pm 0.07	671.39 \pm 0.29	644.72 \pm 0.43	49.01 \pm 0.33	1.57 \pm 0.03	DR4	46342
J2046+506	311.61 \pm 0.05	50.65 \pm 0.09	285.26 \pm 0.25	266.13 \pm 0.21	39.82 \pm 0.21	2.95 \pm 0.05	HB21	52400
J2051+300	312.85 \pm 0.04	30.01 \pm 0.08	191.25 \pm 0.24	177.54 \pm 0.51	25.73 \pm 0.33	1.23 \pm 0.06	Cygnus Loop	29773
J2103+766	315.77 \pm 0.41	76.63 \pm 0.09	68.78 \pm 0.14	57.08 \pm 0.11	24.72 \pm 0.10	3.07 \pm 0.05	-	110618
J2118+608	319.75 \pm 0.09	60.88 \pm 0.06	96.04 \pm 0.07	89.62 \pm 0.13	12.08 \pm 0.09	1.21 \pm 0.03	3C430	56715
J2124+251	321.25 \pm 0.03	25.12 \pm 0.08	128.30 \pm 0.13	120.52 \pm 0.24	14.55 \pm 0.16	1.26 \pm 0.05	3C433	23010
J2145+281	326.39 \pm 0.05	28.16 \pm 0.09	59.12 \pm 0.18	52.60 \pm 0.11	16.92 \pm 0.15	4.77 \pm 0.15	3C436	11360
J2157+380	329.30 \pm 0.04	38.04 \pm 0.08	114.55 \pm 0.12	116.94 \pm 2.86	12.56 \pm 0.40	-0.27 \pm 0.31	3C438	30219
J2247+397	341.79 \pm 0.03	39.73 \pm 0.08	150.89 \pm 0.15	161.54 \pm 0.27	19.69 \pm 0.19	-1.37 \pm 0.04	3C452	26727

continued ...

... continued

Label	Ra [$^{\circ}$]	Dec [$^{\circ}$]	Flux density [Jy]	Location ξ	Scale ω	Shape α	Name	Measurements #
J2339+271	354.98 ± 0.04	27.10 ± 0.07	119.61 ± 0.18	116.70 ± 3.34	16.11 ± 0.57	0.25 ± 0.28	3C465	17031

Table A1: The first 10 source, as an example, of the AARTFAAC northern hemisphere catalogue at 60MHz. The full catalogue as a machine readable csv is available online. The labels here are derived from the positions measured, as in the VLSSr, the positions are given in degrees with the uncertainty calculated from the standard deviation of the individual position measurements. The flux density values, and uncertainties, are calculated from the mode of a skew-normal distribution fit to the population of measurements. The parameters of the skew normal are given. Common names are given to matching sources where possible. Lastly the number of images from which the lightcurve is generated is given.

APPENDIX B: SUPPLEMENTARY ONLINE MATERIAL: HELMBOLT SPECTRA COMPARISON

Here the flux density as measured by AARTFAAC, open circles, are compared to the measurements and spectral fits by [Helmboldt et al. \(2008\)](#), the red dots are the measured flux densities, the dashed lines are power law fits, and the solid lines power laws with turnover at lower frequencies. Some sources have not had any spectra fit, while others are clearly bad fits. In all cases these are taken directly from [Helmboldt et al. \(2008\)](#), without considering the AARTFAAC flux density value, for comparison purposes. For additional comparisons, the plot of Tycho supernova remnant, top left, includes single dish measurements made by [Klein et al. \(1979\)](#), blue circles. Lastly, where source associations could be made the 8C catalogue ([Rees 1990](#)) flux density values are plotted (green circles.) Given that the AARTFAAC catalogue was bootstrapped entirely from eight [Perley & Butler \(2017\)](#) sources, proper agreement across this broad range of sources is an excellent, independent, test of the validity of the calibration method, and the flux density scaling.

This paper has been typeset from a $\text{\TeX}/\text{\LaTeX}$ file prepared by the author.

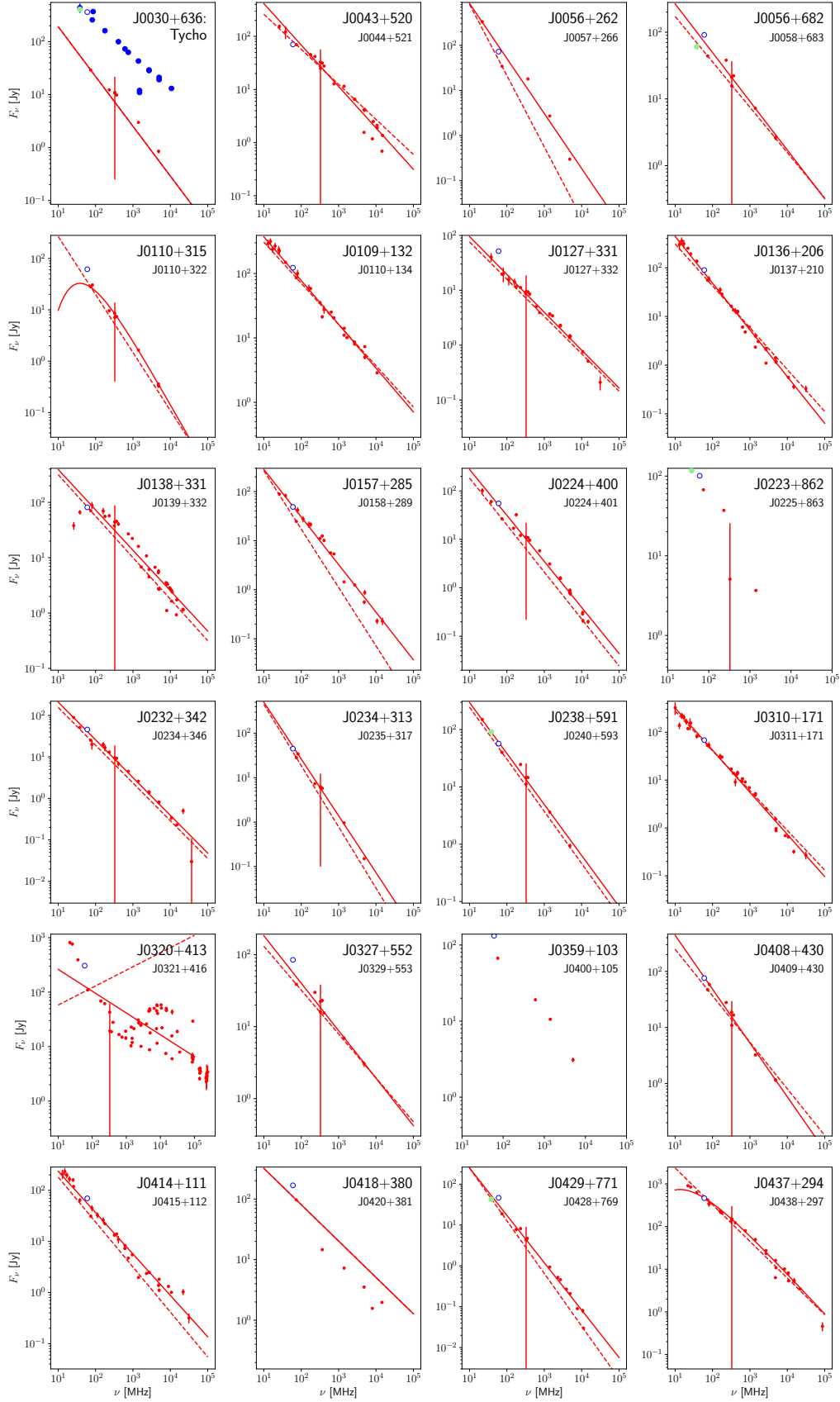


Figure B1. Here the flux density as measured by AARTFAAC (open circles) are compared to the measurements and spectra fit by Helmbolt et al. (2008) (red dots and lines) measurements by Klein et al. (1979) (blue circles) and Rees et al. (1990) (green circles). The larger label refers to the designation assigned by Helmbolt et al. (2008), and the smaller label below is the label in the AARTFAAC catalogue.

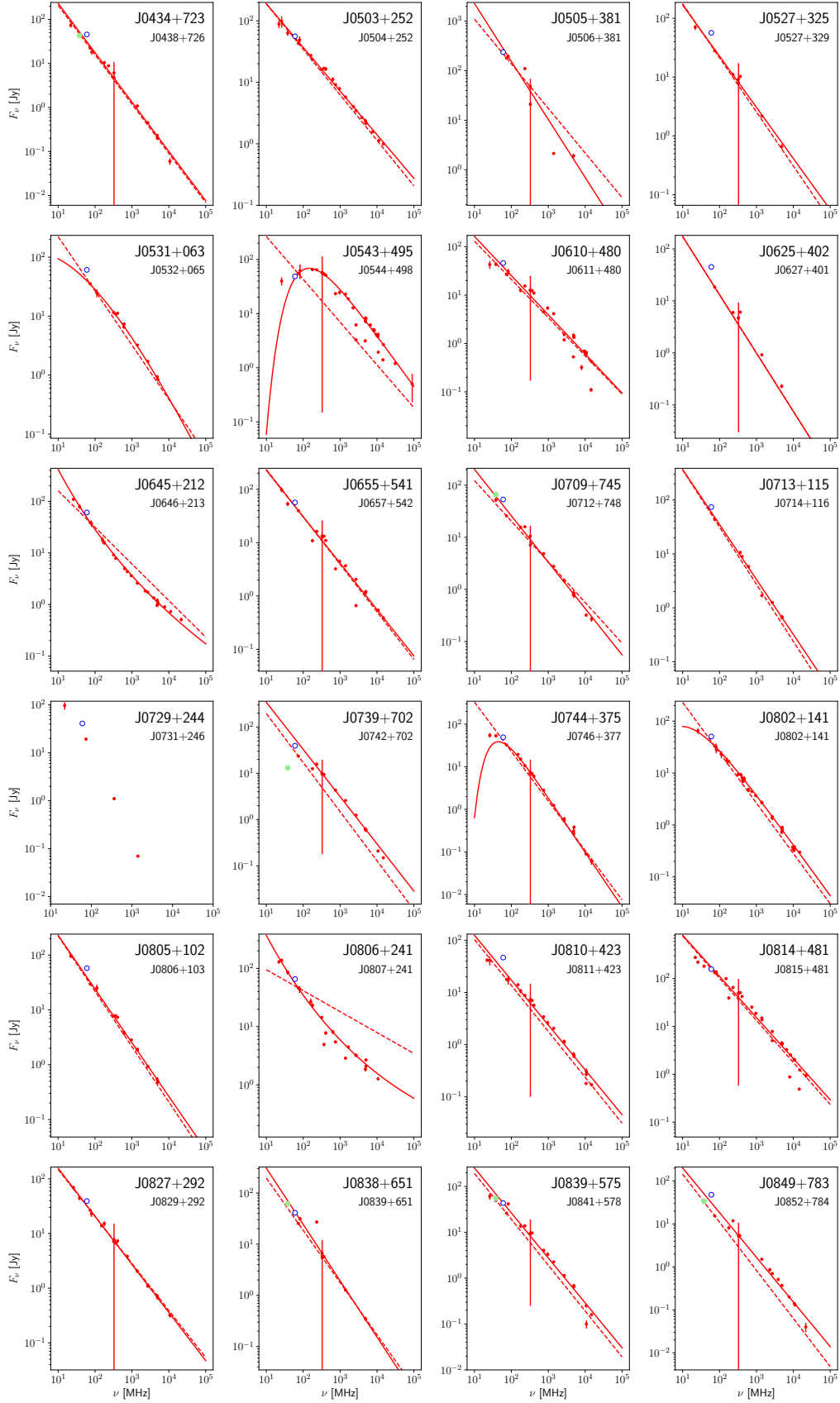


Figure B2. Here the flux density as measured by AARTFAAC (open circles) are compared to the measurements and spectra fit by Helmbolt et al. (2008) (red dots and lines) measurements by Klein et al. (1979) (blue circles) and Rees et al. (1990) (green circles). The larger label refers to the designation assigned by Helmbolt et al. (2008), and the smaller label below is the label in the AARTFAAC catalogue.

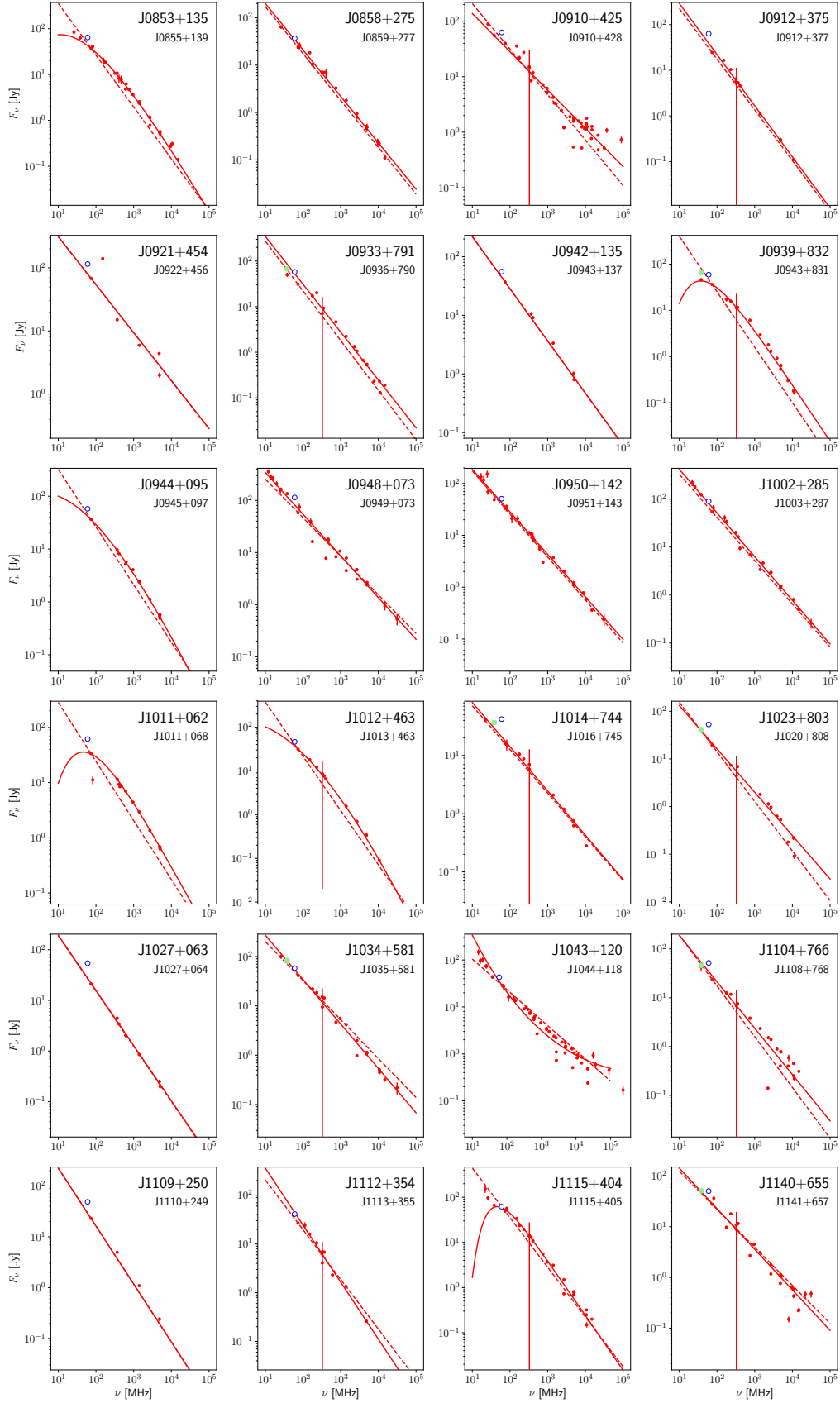


Figure B3. Here the flux density as measured by AARTFAAC (open circles) are compared to the measurements and spectra fit by Helmbolt et al. (2008) (red dots and lines) measurements by Klein et al. (1979) (blue circles) and Rees et al. (1990) (green circles). The larger label refers to the designation assigned by Helmbolt et al. (2008), and the smaller label below is the label in the AARTFAAC catalogue.

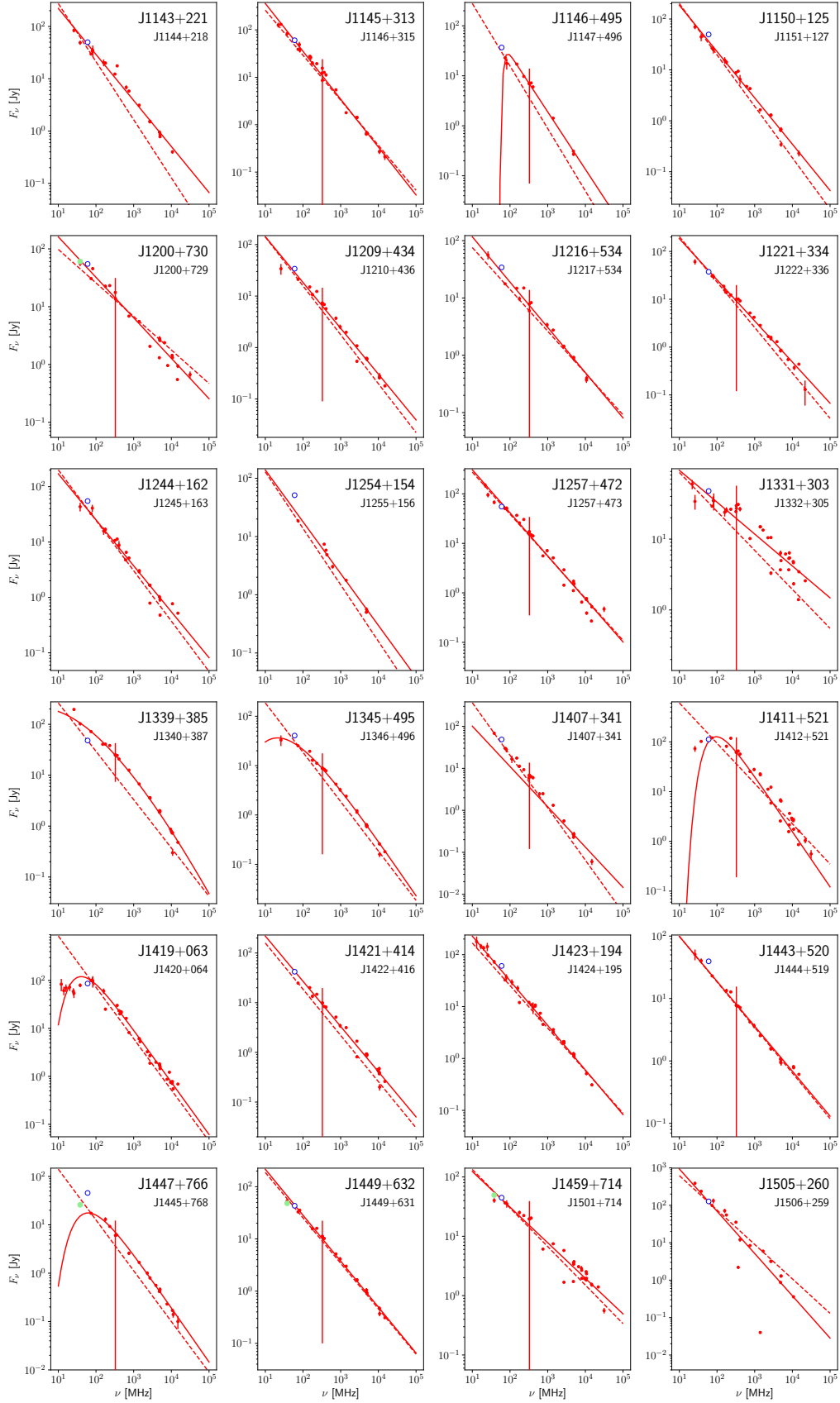


Figure B4. Here the flux density as measured by AARTFAAC (open circles) are compared to the measurements and spectra fit by Helmbolt et al. (2008) (red dots and lines) measurements by Klein et al. (1979) (blue circles) and Rees et al. (1990) (green circles). The larger label refers to the designation assigned by Helmbolt et al. (2008), and the smaller label below is the label in the AARTFAAC catalogue.

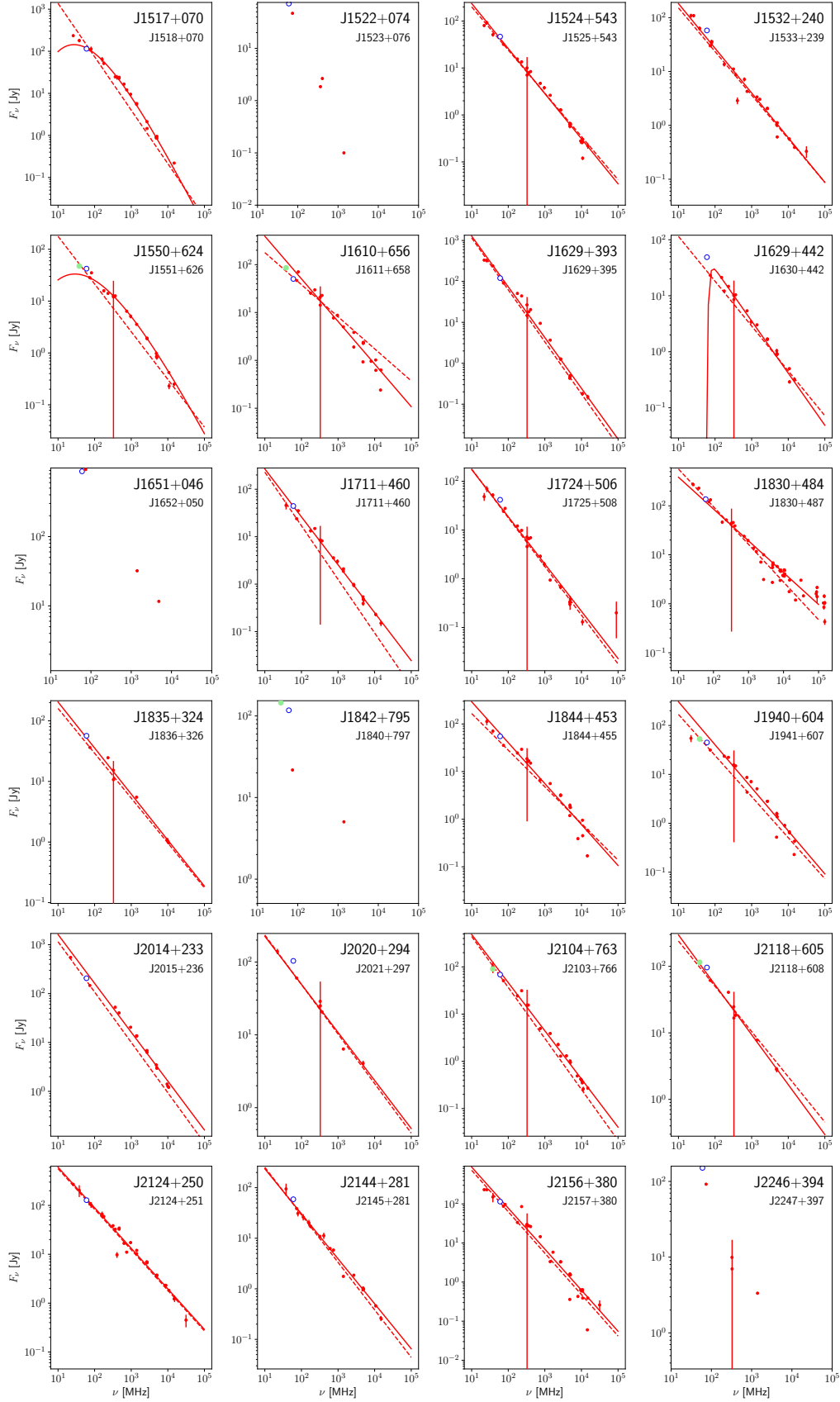


Figure B5. Here the flux density as measured by AARTFAAC (open circles) are compared to the measurements and spectra fit by Helmbolt et al. (2008) (red dots and lines) measurements by Klein et al. (1979) (blue circles) and Rees et al. (1990) (green circles). The larger label refers to the designation assigned by Helmbolt et al. (2008), and the smaller label below is the label in the AARTFAAC catalogue.